BzKs in GOODS-N:

$z \sim 2$ star forming galaxies

by

Nicole Meger

B.Sc. (Honours Physics and Astronomy) The University of British Columbia, 2006

A THESIS SUBMITTED IN PARTIAL FULFILMENT OF
THE REQUIREMENTS FOR THE DEGREE OF

Master of Science

in

The Faculty of Graduate Studies

(Physics and Astronomy)

The University Of British Columbia

December 2008

Abstract

This thesis presents new deep near-infrared imaging data in one of the most well studied regions of the sky, the Great Observatories Origins Deep Survey's northern field (GOODS-N). In particular, we have produced a science-grade K_s-band (2.2 μm) source catalogue with a depth of K_s(AB) = 23.8 magnitudes. With our K-selected sample, we use the BzK two-colour selection criterion to find galaxies lying at redshifts between 1.4 and 2.5. We investigate the redshift distribution of these BzKs using spectroscopic redshifts as well as a new photometric redshift catalogue and find respectively, 13% and 14% contamination from low redshift interlopers. We then compare the relationship between star formation rate and stellar mass with three different star formation rate estimators, derived from the rest-frame ultraviolet, mid-infrared and radio properties. We obtain similar relationships from each of these methods and discuss the inherent uncertainty in estimating high redshift star formation rates. Finally, we test the BzK selection method with two extreme $z \sim 2$ galaxy populations. The BzK criterion is able to select submillimetre galaxies at redshifts from 1.4 to 2.5 even though they have extreme star formation rates, and it can also effectively select highly dust obscured galaxies.

Table of Contents

List of Tables

List of Figures

Acknowledgements

I would like to thank my supervisor, Douglas Scott, for his advice, guidance, confidence and generous use of red ink. I have truly valued the opportunity to travel to various conferences, meetings and observing runs. I have also appreciated all the input and guidance I have received from Alexandra Pope including help with stellar mass estimates, infrared luminosity measurements and our collaboration on SMGs and DOGs. I am grateful to Mark Dickinson for sharing his extensive knowledge of near-infrared observations and galaxy evolution. I would also like to thank Emanuele Daddi for passing along his BzK expertice, Lihwai Lin and Chi Hung Yan for their tireless work on the data reduction, Mark Brodwin for developing the new photometric redshift catalogue, Glenn Morrison for doing the radio stacking and Luc Simard for obtaining the K_s-band observations. I must thank my family, friends and especially my officemates who have managed to keep me sane. And finally, David Slater who has been supportive to the bitter end and will be immensely relieved when this is all over.

Chapter 1

Introduction

The very early Universe was extremely homogeneous and isotropic. Since then, matter has gathered into filaments and clumps forming a cosmic web of large scale structure (Bond et al., 1996). This structure is reproduced by simulations of cold (non-relativistic) dark matter halos undergoing hierarchical merging due to gravitational attraction starting with initial density perturbations which are of the sort produced in an early period of inflation (e.g. Peacock, 1999). The Universe is very well described by a model which includes radiation, normal baryonic matter, cold dark matter (CDM) and some form of dark energy (often denoted by Λ). These components make up the standard model of cosmology, ΛCDM.

Visible matter appears to trace the distribution of dark matter on large scales, but the detailed picture of how the galaxies themselves form and evolve is not as well understood. Hierarchical merging of galaxies cannot fully describe the observed galaxy populations. Rather, we observe 'downsizing' (Cowie et al., 1996) in the star formation history of the Universe: statistically speaking, massive galaxies form their stars earlier than small galaxies. Although the evolution of the collisionless dark matter is well understood, the complexities of 'gastrophysics' are much more challenging to model. As a result, theorists rely on simple prescriptions for assigning galaxy properties to dark matter halos (so called 'semi-analytic galaxy formation'). The range of length scales and physical processes involved means that it has not been possible to construct an *ab initio* calculation of how galaxies form and evolve.

1.1 Cosmology

The Universe is expanding. The farther away a galaxy is, the faster it is moving away from us and the more redshifted the light from that galaxy becomes. For a given redshift (z), we can relate the emitted and the observed wavelength (λ) and frequency (ν):

$$1 + z \equiv \frac{\lambda_{\rm obs}}{\lambda_{\rm em}} = \frac{\nu_{\rm em}}{\nu_{\rm obs}}. \tag{1.1}$$

Since more distant objects have higher redshifts and light travels at a constant speed, we see distant objects at earlier times and observed redshift is a monotonically decreasing function of time. In order to determine an observed flux from the emitted luminosity we must redshift the wavelength of the radiation but also include the effect of distance dimming through the luminosity distance ($D_{\rm L}$). This is a function of redshift and the parameters of the specific cosmological model:

$$D_{\rm L} = (1+z)\frac{c}{H_0}\int_0^z \frac{dz}{\sqrt{(1-\Omega)(1+z)^2 + \Omega_\Lambda + \Omega_{\rm m}(1+z)^3 + \Omega_{\rm r}(1+z)^4}}. \tag{1.2}$$

Here, Ω_Λ, $\Omega_{\rm m}$ and $\Omega_{\rm r}$ are respectively, the density (ρ) of dark energy, matter and radiation divided by the critical density ($\rho_{\rm c} = \frac{3H_0^2}{8\pi G}$) of the Universe and $\Omega \equiv \Omega_\Lambda + \Omega_{\rm m} + \Omega_{\rm r}$, while H_0 is the present-day expansion rate of the Universe. We use $H_0 = 73\,{\rm km\,s^{-1}\,Mpc^{-1}}$, $\Omega_{\rm m} = 0.3$ and $\Omega_\Lambda = 0.7$ (Spergel et al., 2007).

The emitted luminosity density can be computed via:

$$\nu_{\rm em} L_{\nu_{\rm em}} = \nu_{\rm obs} L_{\nu_{\rm obs}} = (4\pi D_{\rm L}^2)\nu_{\rm obs} S_{\nu_{\rm obs}}. \tag{1.3}$$

In this thesis, optical and near-infrared photometry are measured in magnitudes. We use AB magnitudes except when explicitly stated (Oke, 1974). We convert between AB magnitude and flux density ($_\nu S$) through the following equation:

$$m_{\rm AB} = -2.5\log(S_\nu[{\rm W\,m^{-2}\,Hz^{-1}}]) - 56.1. \tag{1.4}$$

1.2 The star formation history of the Universe

We would like to have a coherent picture of how the first collapsed halos and stars evolve into the types of galaxies we have in the Universe today. We can piece together an empirical picture of galaxy evolution by detecting large samples of distant galaxies and comparing how various physical properties change throughout cosmic time. Imaging and spectroscopy in different wavebands allow us to determine characteristics such as morphology, stellar and dynamical mass, space density, nuclear activity and star formation rate.

The popular Lilly-Madau plot (Lilly et al., 1996; Madau et al., 1996) tracks star formation density over time. Since its conception in 1996, many studies have estimated the total star formation density at various redshifts (e.g. Baldry et al., 2005; Thompson et al., 2006; Reddy et al., 2008). For a recent Lilly-Madau plot, see figure 7 in Pérez-González et al. (2008), which compares results of several studies. Star formation measurements agree very well up to $z \sim 1$ but by $z \sim 2$, the scatter significantly increases. High redshift galaxies are difficult to identify and once identified their star formation is complicated to measure. Using the BzK cirterion to select $z \sim 2$ galaxies and multi-wavelength data to determine their star formation rates will help determine the star formation history at higher redshifts.

1.3 Observing $z \sim 2$ galaxies

At $z \sim 2$, the locally well-understood, bright optical part of galaxy emission is redshifted into the near-infrared (NIR). Powerful NIR imagers have only recently become available, allowing for deep surveys to be carried out. Since these galaxies are often optically faint, we cannot rely on spectroscopy to identify their redshifts. Instead, we use multi-wavelength data including NIR for photometric selection approaches which can be tuned for particular redshift ranges (e.g. Steidel et al., 1996; Elston et al., 1988; Erb et al., 2003; Daddi et al., 2004).

We count on photometry to not only select $z \sim 2$ galaxies, but also to quantify their physical characteristics. Synthesizing multi-wavelength data gives an overall picture of the energy output of a galaxy, called the spectral energy distribution (SED). SEDs can be modelled by inputting many parameters, such as initial mass function, metallicity, stellar mass, star formation rate, star formation history and dust content (Bruzual & Charlot, 2003). The initial mass function (IMF) describes the distribution of stellar masses which are formed. For our work, we use the standard Salpeter IMF (Salpeter, 1955). The metallicity is a measure of the fractional mass of elements heavier than helium. Stellar mass is dominated by old stars and so to estimate it we must measure the amount of light coming from $\sim 1.6\,\mu$m in the rest-frame (Sawicki, 2002). To quantify the current star formation rate (SFR), we need to measure the amount of light coming from young stars. Disentangling how much light comes from young stars relative to the old stars gives a sense of the star formation history which can be determined more comprehensively by synthesizing spectra coming from stars of varying ages (Bruzual & Charlot, 2003). Dust complicates these measurements since

it absorbs optical and UV radiation and re-emits in the infrared.

We calibrate relationships to convert between flux density and star formation rate using local galaxies which can be observed in great detail (e.g. Calzetti et al., 2000). However, there are complications in applying locally calibrated relationships to distant galaxies. For example, IMF and dust extinction both depend on metallicity, which is usually not very well constrained in distant galaxies (Calzetti, 2008a). One way to understand how reliable these estimates are is to compare various methods of determining the same characteristic, such as SFR, and attempt to understand their differences. Thus, we should be able to understand whether there are simple and effective methods of estimating SFR directly from photometry.

1.4 Great Observatories Origins Deep Survey

The Great Observatories Origins Deep Survey (GOODS; Giavalisco et al., 2004) was conceived to focus the efforts of NASA's three major space telescopes (*HST*, *Chandra* and *Spitzer*) on the same two areas of the sky to produce the best wavelength coverage possible. The two fields were chosen to be quite unremarkable and therefore, presumably representative of the deep Universe in general. To enable follow-up by all the world's telescopes, one field was chosen in each of the two hemispheres. The northern field selected is the Hubble Deep Field North (HDFN) and the southern field is the Chandra Deep Field South (CDFS), GOODS-N and GOODS-S respectively. GOODS-N is a $10' \times 16'$ field centred at $12^{\rm h}36^{\rm m}55^{\rm s}$, $+62°14'15''$ (Giavalisco et al., 2004). Since the project's conception, the GOODS fields have also been targeted by many ground-based telescopes.

This thesis focuses on new observations in GOODS-N at near-infrared (NIR) wavelengths. Prior to our data from WIRCam on CFHT (discussed at length in chapter 2), the best available NIR data on GOODS-N were from FLAMINGOS on KPNO (Elston et al., 2003), which are significantly shallower than the NIR data on GOODS-S from ISAAC on the VLT (Moorwood et al., 1998). Figure 1.1 shows the NIR depths compared to the multi-wavelength sensitivities of the GOODS-N optical data from both *HST* and Subaru and the infra-red data from *Spitzer*. The GOODS-N NIR data are now comparable to that of GOODS-S.

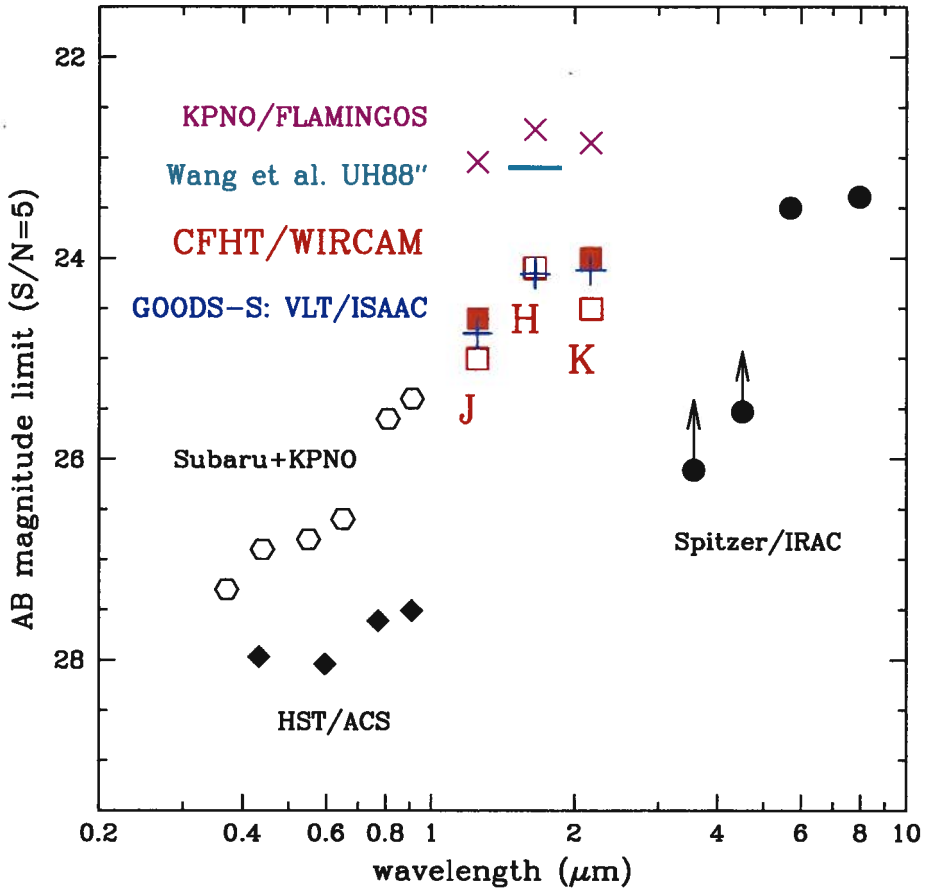

Figure 1.1: Multi-wavelength sensitivities of GOODS data. Solid red squares show current GOODS-N depths. Open squares show expected depths from proposed 2009A observations for H- and J-band and with the inclusion of UH data to become publicly available for K-band.

Chapter 2

Data

This thesis was motivated by the efforts of the GOODS collaboration to fill in the near-infrared (NIR) gap in the multi-wavelength coverage for GOODS-N. This chapter describes the NIR camera we used, the data reduction and catalogue extraction processes and finally summarizes the multi-wavelength data available in GOODS-N.

2.1 The Wide-field Infra-Red Camera

The Wide-field Infra-Red Camera (WIRCam) (Puget et al., 2004) on the Canada France Hawaii Telescope (CFHT) is a NIR imager which began taking data in the 2006A semester. WIRCam has J, H and K_s broad-band NIR filters shown in figure 2.1, centred at 1.25, 1.65 and 2.15 μm. The camera has a $21.5' \times 21.5'$ field-of-view and is fully-sampled at $0.3''$ per pixel. The camera includes four 2048×2048 HAWAII2-RG CCDs (referred to as 'chips' hereafter). The chips have $45''$ gaps between them, but dithering allows for a nearly uniform exposure time over the whole area.

In 2006A, members of the GOODS collaboration attempted to fill the NIR gap in the multi-wavelength coverage of GOODS-N. A joint effort submitted proposals to both the Canadian and Taiwanese agencies by P.I.'s Luc Simard and Lihwai Lin, respectively. Canadian time was awarded for observations in the K_s-band (06AC33) while Taiwanese time was used for the J-band (06AT02). In 2006A a Hawaiian group (P.I. Len Cowie) also obtained K_s-band observations (06AH45 and 06AH96) in GOODS-N, which were released at the end of February 2008 after an extended proprietary period due to delays at Terapix affecting all WIRCam data. The Hawaiian group continues to receive time to observe the field in K_s; their 2007A data (07AH36) are scheduled to be released in February, 2009, while their 2008A data (08AH25) will be released in August, 2009. Our Taiwanese collaborators received more time to observe in J in 2007A (07AT18 and 07AT19).

This thesis will focus on the K_s (referred to as simply "K" hereafter) data, though the reduction effort has been carried out in parallel for both K and J.

2.2 Data Reduction

In the first stack that we received, data were pre-processed at CFHT by the 'I'IWI pipeline developed by Loic Albert for WIRCam data. The individual images were then sent to Terapix in France to be stacked and distributed. A hardware issue caused early WIRCam observations to have cross-talk artifacts appearing as a repeating pattern (often donut-shaped) above and below every bright source. The first stacks received from Terapix also had large scale background gradients and bright star-tracks. The astrometry was quite good in the central GOODS-N region, but the extended region had significant astrometric residuals (as large as $1''$). For early analysis, we simply masked out large regions of the image around bright objects and worked in the central GOODS-N region. In the first such reduction, we reached a 5σ depth of $K(\mathrm{AB}) = 23.5$ with 10.4 hours of integration time.

Our collaborators in Taiwan then took over data reduction in an attempt to improve on the Terapix release. Lihwai Lin and Chi-Hung Yan worked with Wei Hao Wang to develop a reduction script to reduce crosstalk. This program finds the brightest sources and then removes excess signal from every 16 pixels above and below each source. The 16 pixel offset corresponds to the fact that after reading out, the detector is reset in 16 line blocks.

During the stacking process, individual frames are transformed by matching to 2MASS sources (Skrutskie et al., 2006). Since GOODS-N is well out of the Galactic Plane and saturates for the brightest stars, there are only about 100 stars over the whole field which can be used to make the transformation. Using the SDSS catalogue (York et al., 2000) instead of 2MASS significantly reduces the mean astrometric offset. Although there are still some large residuals in the lower right corner of the image which we do not understand, the majority of the image has very accurate astrometry ($< 0.15''$). It is possible that there are slight differences between each of the four chips on the detector, explaining why one corner of the image is not as consistent. Small chip effects are also seen in the photometry but these effects are small (typically below 1σ) and can be ignored.

After crosstalk removal and pre-processing with 'I'IWI, stacking is done with SCAMP and SWARP developed by Terapix. We have now settled on a reduction procedure resulting in a version 1.0 data image. This stack includes 06AC33 and 06AH45, but leaves out images with poor seeing, including all of 06AH96 ($\sim$ 2 hours), giving a total of 16.6 hours of integration time. Details on the data reduction procedure will be published in Lin et al. (in preparation). We reach a 5σ depth of 23.8, 0.3 magnitudes deeper than the original Terapix stack.

2.3 Making the Source Catalogue

All photometry is carried out using SExtractor (Bertin & Arnouts, 1996). To calibrate the WIRCam photometry, we compare against other available K data. For an absolute zero-point calibration we use the 2MASS catalogue. As discussed for the astrometry, there are only about 100 unsaturated sources in both GOODS-N and the 2MASS catalogue. However, this is less of a problem for calibrating the photometry since we can average over all the available sources, whereas for calibrating the astrometry all the sources are used to define the transformation. The 2MASS catalogue is in Vega magnitudes, so in order to set an absolute zero-point in the AB system, we use the WIRCam K-band filter transmission curve to calculate the conversion $K(\mathrm{AB}) = K(\mathrm{Vega}) + 1.844$. Comparing `mag_auto` measured in the WIRCam image with the 2MASS magnitude, we find an absolute zero-point of 31.915 for the stack.

To calibrate the photometry for faint sources, we use the FLAMINGOS JHK_s data (Elston et al., 2003). We check for colour gradients in the comparison between the WIRCam and FLAMINGOS data. Any differences are within the 1σ level, so we are confident in the quality of the WIRCam photometry.

We take the approach of detecting all sources and then making a cut to select only the significant sources from the catalogue. The full catalogue includes all sources with at least three pixels 1σ above the local background to avoid including cosmic rays. We can then set a threshold cutoff at the desired signal-to-noise ratio (SNR):

$$m = -2.5\log(S_\nu) + \mathrm{ZP} \tag{2.1}$$

$$\sigma_m = 2.5 \times 0.434 \left(\frac{dS_\nu}{S_\nu}\right) = \left(\frac{1.085}{\mathrm{SNR}}\right). \tag{2.2}$$

The zero-point (ZP) is specific to each image. For the BzK sample selection, we require a 5σ detection in K, meaning $\sigma_m \leq 0.217$. The noise is measured from the local background and uses the weight map we include for each image.

SExtractor outputs internal and external flags. The internal flags indicate photometric quality. In particular, a flag value of 1 indicates nearby neighbours, 2 indicates a blended source, 4 indicates saturated pixels and higher flag values indicate truncation or corruption. We require `flags` < 4

and rely on small (2″ diameter) apertures to measure the flux from each source.

The external flags report objects in areas of the image with problems. These areas are indicated in a flag map which was produced by Lihwai Lin using WEIGHTWATCHER during data reduction. In the flag map, a value of 1 indicates areas with low exposure time, 2 indicates pixels affected by crosstalk and 4 indicates pixels which are saturated and were removed during data reduction, usually at the centres of bright stars. The SEXTRACTOR parameter tracing the highest value of flagged pixel within the object's area is '`imaflags_iso`', which we require to be zero.

2.4 Source counts

As a check on our photometry, we can compare our 5σ K-band catalogue source counts to other K-band data. Figure 2.2 shows our data compared to the FLAMINGOS data on GOODS-N (the best available prior to our observations) and the ISAAC data on GOODS-S. Our number counts are low at the very bright end, since bright objects near saturation were flagged during data reduction and therefore removed from the catalogue. We find that we are in very good agreement with the other two catalogues up to $K \sim 22.5$, where our counts are slightly high compared to the GOODS-S number counts. This could be due to cosmic variance. Since both the GOODS fields are quite small ($\sim$ 160 arcseconds^2), there may be an over density in the northern field compared to the southern field. Our WIRCam data reach a depth of $K(\mathrm{AB}) = 23.8$, comparable to the ISAAC data in GOODS-S.

2.5 GOODS-N multi-wavelength coverage

As discussed in section 1.4, we work in GOODS-N because it has excellent multi-wavelength coverage. Infrared observations by *Spitzer* include the four IRAC bands at 3.6, 4.5, 5.8 and 8.0 μm, as well as the MIPS 24 μm imaging (Dickinson et al. in preparation). 2 Ms of integration time with *Chandra* provide a very deep X-ray map (Alexander et al., 2003). There are very deep 1.4 GHz radio data from the VLA (Morrison et al. in preparation). Also, there are submillimetre and millimetre data from JCMT with SCUBA at 850 μm (Pope et al., 2006), AzTEC at 1.1 mm (Perera et al., 2008) and from IRAM with MAMBO at 1.2 mm (Greve et al., 2008).

Very deep optical data exist from ACS on *HST* with high angular resolution (Giavalisco et al., 2004). There are also excellent $BVRIz'$ from the Subaru telescope (Capak et al., 2004). In order to combine the *HST* data with our ground-based NIR observations, the ACS data must be degraded to the WIRCam seeing (0.7″ from 0.05″). The degraded ACS data would then be comparable in depth to the Subaru data. Additionally, both the WIRCam and Subaru data cover an extended region ($\sim 20' \times 20'$) centred on GOODS-N, while the ACS data cover only GOODS-N-proper. Using the Subaru optical data allows us to select a larger sample to be stacked in the radio map which is also larger than GOODS-N-proper. For these reasons we chose to use the ground-based Subaru data.

2.5.1 Redshifts

There are many publicly available spectroscopic redshifts in GOODS-N (Cohen et al., 2000; Cowie et al., 2004; Wirth et al., 2004; Chapman et al., 2005; Reddy et al., 2006). These $\sim$ 1500 redshifts cover GOODS-N-proper. To utilize our full sample area, we use photometric redshifts where spectroscopic redshifts are not available. Mark Brodwin and Lihwai Lin produced a preliminary catalogue of photometric redshifts using the optical and NIR $UBVRizJK$ data from Subaru and WIRCam. The comparison between spectroscopic and photometric redshifts are shown in figure 2.3. The photometric redshifts are very good up to $z \sim 1$, but unfortunately become less reliable at $z \sim 2$ where galaxy spectra are not as well-understood.

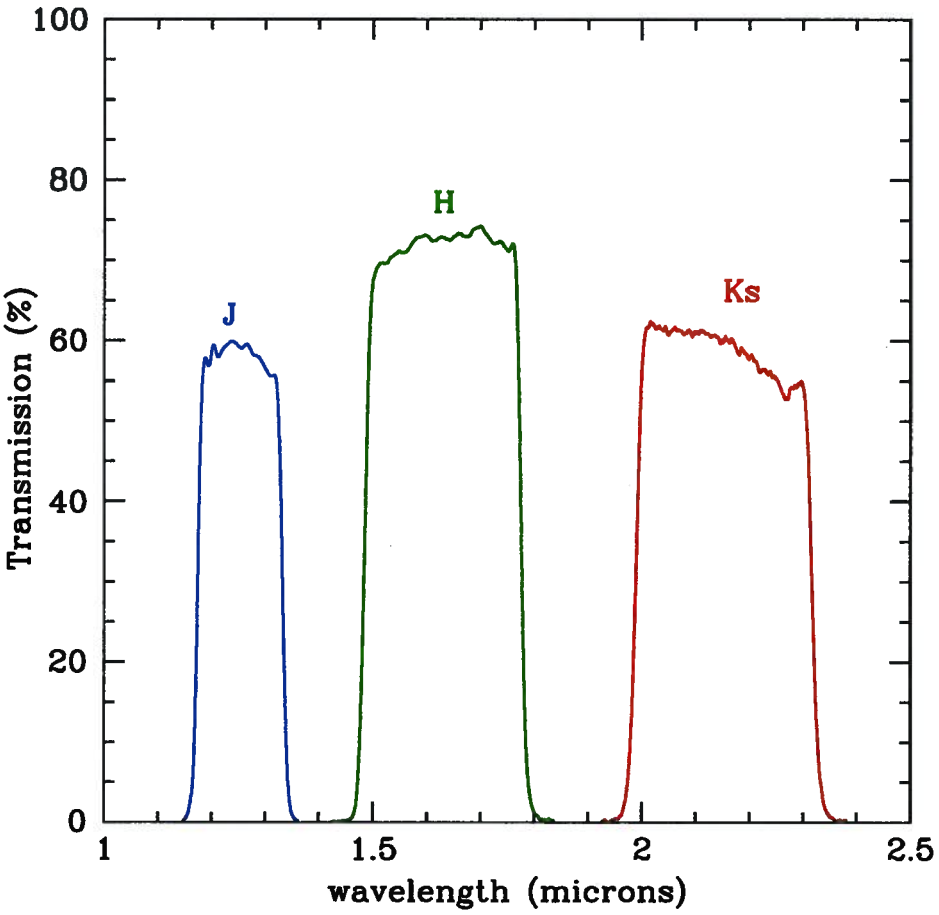

Figure 2.1: Transmission curves for WIRCam's J, H and K_s broad-band filters (Puget et al., 2004).

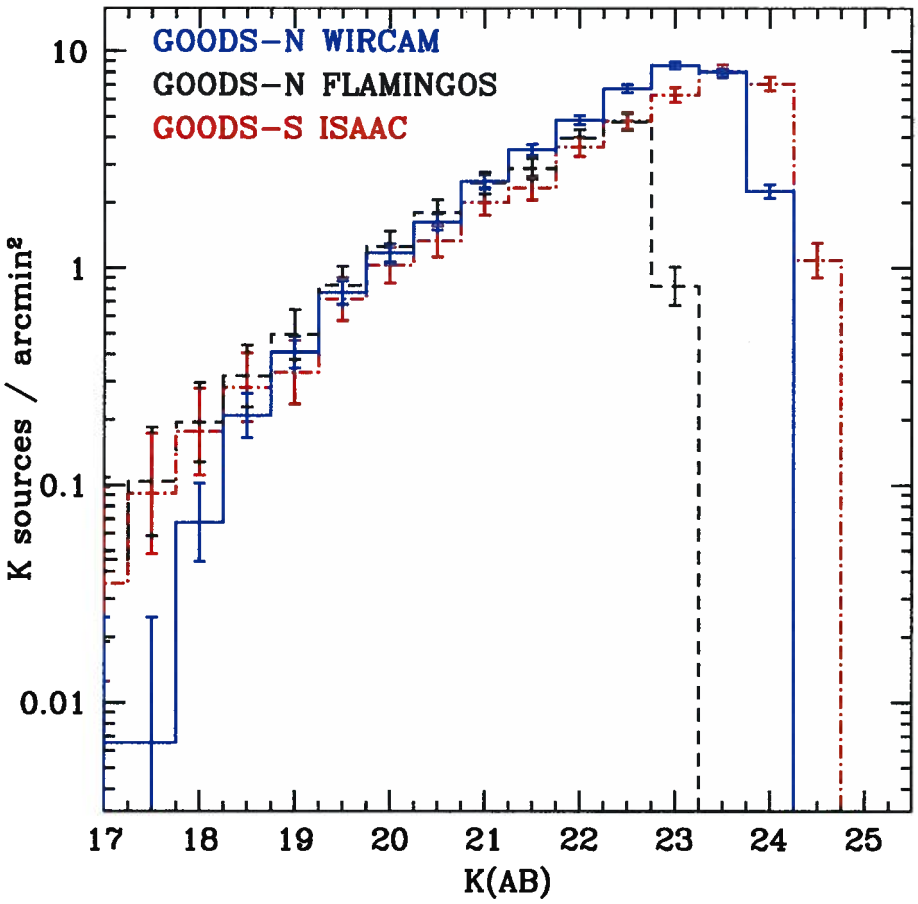

Figure 2.2: Number counts for our WIRCam K-band catalogue compared to the FLAMINGOS data on GOODS-N and the ISAAC data on GOODS-S. Our data are almost 1 magnitude deeper than the FLAMINGOS and are comparable to the ISAAC data.

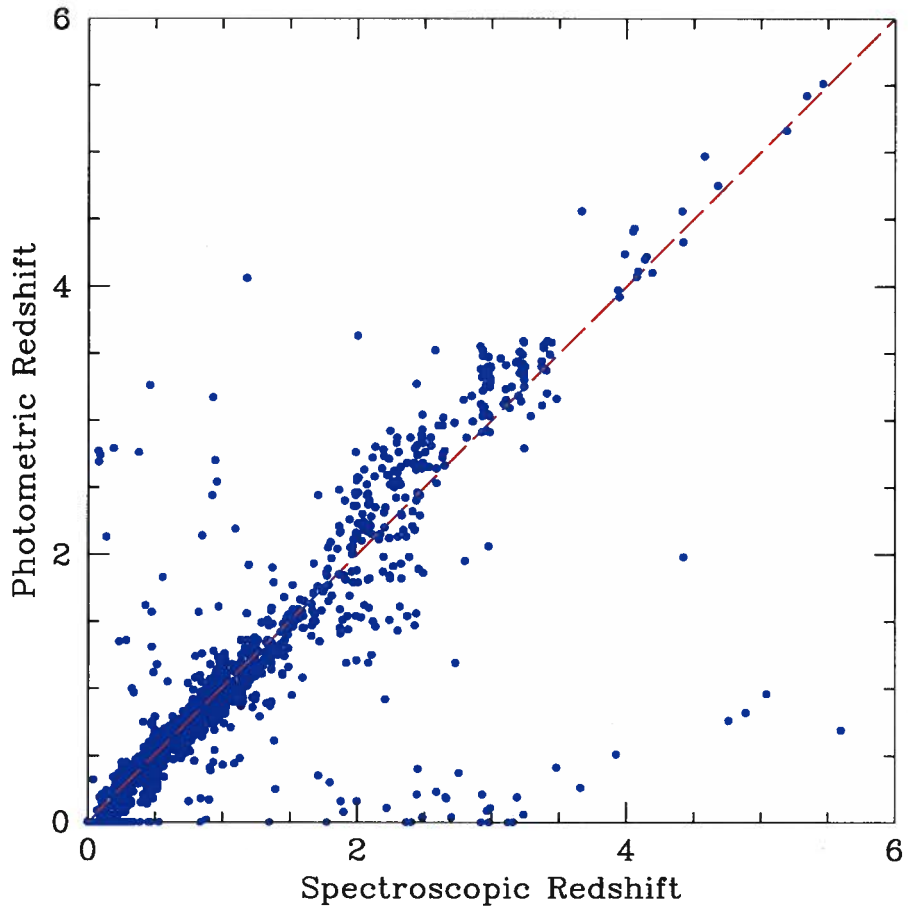

Figure 2.3: Comparison between all available spectroscopic redshifts with our preliminary photometric redshift catalogue. Photometric redshifts were estimated using optical and NIR $UBVRizJK$ data from Subaru and WIRCam in the extended GOODS-N.

Chapter 3

BzK galaxy selection

The BzK criterion was first proposed in Daddi et al. (2004) as a way to select $z \sim 2$ galaxies and differentiate between actively star forming and passively evolving galaxies. For a $z = 1.9$ galaxy, spectral breaks lie to the blue side of the B filter and in between the z and K filters (see figure 2 in Daddi et al. (2004)). The magnitude difference between bands give the flux ratio (see equation 1.4) which we refer to as a colour. Therefore, the location of the two spectral breaks will affect the colours as the galaxy spectrum is redshifted.

The BzK plane is $(z-K)$ versus $(B-z)$, with $BzK \equiv (z-K)-(B-z)$. Actively star forming BzK galaxies (SBzKs) have $BzK \geq -0.2$. This cut in BzK space is roughly parallel to dust reddening effects in galaxy templates allowing for a robust selection independant of dust content (see figure 8 in Daddi et al. (2004)). Passively evolving BzK galaxies (PBzKs) have $BzK < -0.2 \bigcap (z-K) > 2.5$. The BzK redshift range is typically $1.4 \leq z \leq 2.5$, with many of the outliers being hard X-ray sources which are assumed to trace AGN contamination. The BzK selection was developed for galaxies with $K \leq 22$, but here we can push to fainter limits. This chapter describes the photometry, matching to the multi-wavelength data and the redshift distribution we get for our $K < 23.8$ sample.

3.1 Photometry

We use the Subaru telescope B and z data with our WIRCam K imaging in order to measure the $(B-z)$ and $(z-K)$ colours of objects in the extended GOODS-N field. We first align the B and z images to the frame of the K image by matching bright sources to define a transformation and then reprojecting the B and z images onto the K frame. Using SExtractor (Bertin & Arnouts, 1996) in dual-image mode, we detect in K and then measure the flux within the same circular apertures in each image. We use small, $2''$ diameter circular apertures to maximize signal-to-noise for the distant $z \sim 2$ galaxies. However, we must apply some aperture correction to approximate total magnitude. Aperture corrections are derived for each

band from the stellar sequence, for which the PSF is consistent. We use a larger $4''$ diameter circular aperture to approximate the total magnitude. The B, z and K aperture corrections are shown in figure 3.1.

This procedure gives a sample which is magnitude-limited in K. If there is no significant detection in B or z, we measure the background flux and set a 5σ upper limit on the brightness of the source in that band. In this way, we can still place the source on the BzK diagram using

$$m > -2.5\log(5 \times dS) + ZP_{\rm band}, \tag{3.1}$$

with $\mathrm{ZP}_B = 31.046$ and $\mathrm{ZP}_z = 33.826$ taken from Capak et al. (2004). Using these $2''$ diameter circular apertures, the Subaru data reach 5σ depths of $B = 27.5$ and $z = 26.1$. Sources with 5σ detections in K but not in B and/or z are the cyan arrows in Figure 3.2. Objects detected in B but not in z can be classified as SBzKs, and objects detected in z but not in B can be classified as PBzKs, while objects with no detection in either B or z are unclassified (UBzKs).

To account for slight differences between the filters used to set the BzK selection criterion and those on WIRCam and Subaru, we adjust the $(B-z)$ and $(z-K)$ colours by fitting to the stellar sequence in the BzK diagram as suggested in Daddi et al. (2004). This gives the $(B-z)$,$(z-K)$ plane shown in figure 3.2. There are 5588 BzKs with $\geq 5\sigma$ detections in B, z and K. This number splits into 5563 SBzKs and 25 P$BzKs$. There are 989 BzKs with $\geq 5\sigma$ detections in K but not in one or both of B and z: 200 SBzKs, 55 PBzKs and 734 unclassified BzKs. The total number of BzK-selected galaxies is 6577.

3.2 Matching to multi-wavelength data

We match to all available data described in section 2.4. We search for matches within $1.0''$ except for IRAC and MIPS catalogues, for which we choose a smaller matching radius of $0.5''$ to avoid blending issues. The WIRCam data cover 900 arcmin^2, but we restrict the BzK selection to the central 700 arcmin^2, which has more significant exposure time. Spectroscopic redshifts are only available in GOODS-N-proper (ie. the $10' \times 16'$ area). The IRAC and MIPS area is $\approx 1/3$ the BzK area and most BzKs have IRAC detections in the overlap region. Table 3.1 shows the breakdown of matching criteria and number of matches.

waveband	match radius ($''$)	area (arcmin^2)	number of matches
X-ray	1.0	400	163
IRAC	0.5	220	2313
MIPS	0.5	220	645
Radio	1.0	900	213
spec-zs	1.0	160	346

Table 3.1: Multi-wavelength catalogues available for GOODS-N, which have been matched with the new BzK catalogue.

3.3 Redshift distribution

The BzK criterion was designed to select $1.4 \leq z \leq 2.5$ galaxies, and was originally developed for $K(\mathrm{AB}) \leq 22$ (Daddi et al., 2004). Higher redshift red galaxies will also be selected, but after removing AGN most low redshift galaxies should be excluded. In their initial study, Daddi et al. (2004) found $\sim 12\%$ contamination from low redshift 'interlopers'. There has been evidence in other BzK studies which suggest that the redshift range widens for deeper surveys (e.g. Reddy et al., 2005). In particular, Dunne et al. (2008) find $\sim 30\%$ of BzKs have $z < 1.4$ for their $K \leq 24.9$ BzK sample with photometric redshifts.

In order to test the BzK selection redshift distribution, we first match to the entire sample of available spectroscopic redshifts. The resulting distribution is shown in the top left panel of figure 3.3. In general, the BzK selection does very well, as the distribution obviously peaks within the $1.4 \leq z \leq 2.5$ range. We find 17% of galaxies with BzK colours are at $z < 1.4$, but this fraction improves to 13% when we remove hard X-ray sources. Not surprisngly, the contamination increases with the depth of the sample as seen in the top right hand panel of figure 3.3. The hard X-ray detections do not identify any low redshift AGN for $K > 22$.

We considered the possibility that the extent of the contamination we observe in the redshift distribution is partially a selection effect. It is easier to obtain spectroscopic redshifts for low redshift galaxies, so perhaps $z < 1.4$ galaxies are over-represented in the GOODS-N spectroscopic catalogues. In order to investigate such selection effects, we also compare to the TKRS catalogue (Team Keck Treasury Redshift; Wirth et al., 2004), which is flux-limited in R. Only 58 BzKs have TKRS redshifts and 30% of those are at $z < 1.4$. This R-limited catalogue is almost entirely below $z = 1.5$ and therefore is of little help in assessing selection biases in our K-limited sample.

We then match to our *preliminary* photometric redshift catalogue. This

distribution is shown in the lower left panel of figure 3.3. As with the spectroscopic sample, notice the sharp drop in BzKs at the $z = 1.4$ boundary. In this case, the drop in the distribution is more gradual, due to uncertainty in the photometric redshifts. The low redshift contamination is still only 14%. There are many high redshift galaxies included, but here the photometric redshifts are very uncertain. Notice in the bottom right panel of figure 3.3, that removing hard X-ray sources does not help much at these depths, due to the X-ray detection limit. Another method of identifying AGN is with the *Spitzer* colour diagrams (e.g. Sajina et al., 2005) but extremely deep infrared data are required. The photometric redshift sample shows a large peak at $z = 1.5$. This is likely an artifact of the photometric redshift routine.

For both the spectroscopic and photometric redshift samples, the average redshift is $z = 1.9$. This average value is used in section 4.2.3 in the radio stacking analysis.

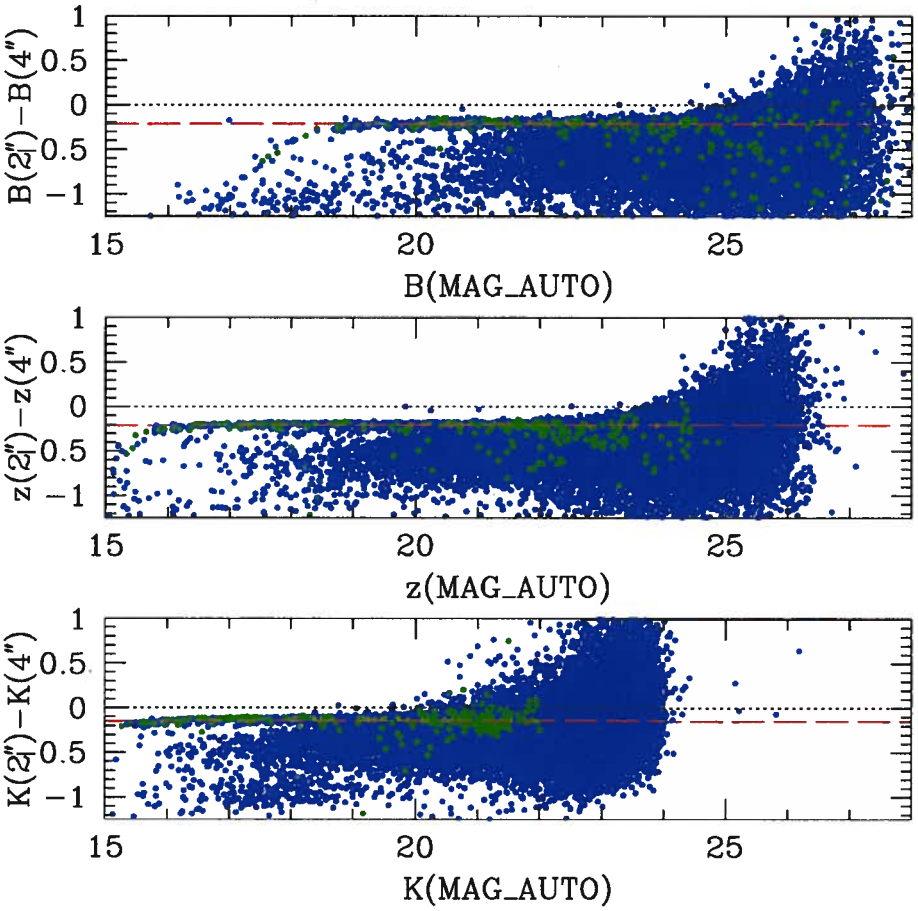

Figure 3.1: Derivation of aperture corrections for each of B, z and K. The green points are classified by SExtractor as stars (ie. setting the 'star_class' parameter to 1) in K. Averaging $m(2'') - m(4'')$ for the unsaturated stars gives the aperture corrections, which are shown by the dashed red lines.

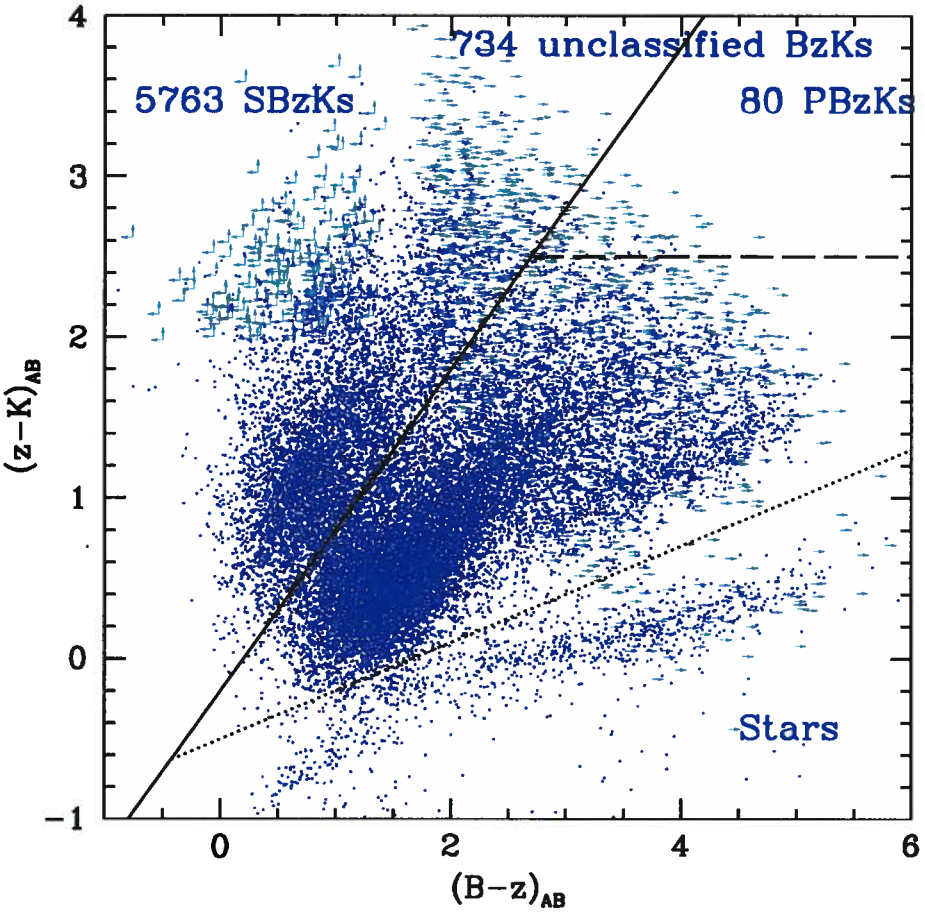

Figure 3.2: BzK diagram for GOODS-N using WIRCam K_s and Subaru B and z' photometry. This is designed to select $1.4 \leq z \leq 2.5$ galaxies and to differentiate between actively star forming and passively evolving sources. Galaxies with $(z-K)-(B-z) > -0.2$ (upper left corner) are star forming (SBzKs), while those with $(z-K) > 2.5$ (upper right corner) are passive (PBzKs). Cyan arrows show those galaxies detected in K but not in either B or z. Galaxies detected only in K are not shown, but are included in the total number of unclassified BzKs (UBzKs). Stars (lower right) are fit to the stellar sequence of Daddi et al. (2004) to account for slight differences in the filters used here and those used to design the BzK selection.

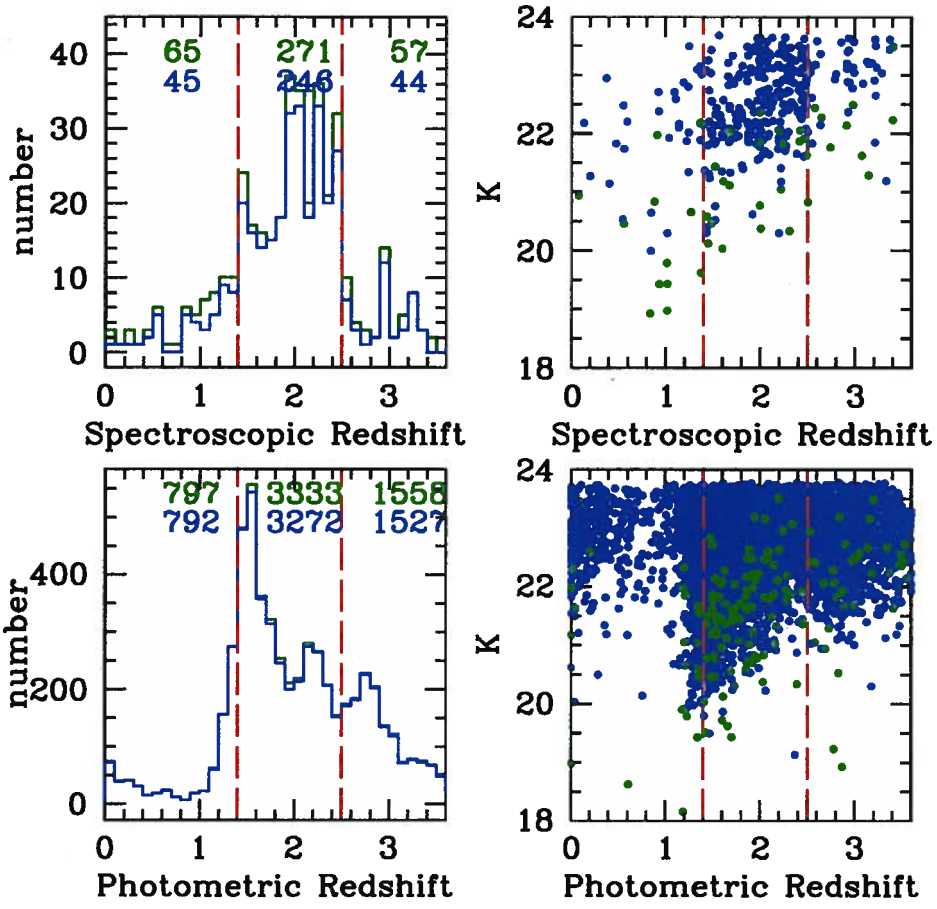

Figure 3.3: Redshift distributions for BzKs with spectroscopic redshifts (top panels) and photometric redshifts (bottom panels). Left panels show histograms, while right panels show the redshift dependence on K. Green shows sources with hard X-ray detections. Red dashed lines delineate the BzK redshift range of $1.4 \leq z \leq 2.5$.

Chapter 4

Star formation rate estimators

4.1 Stellar mass

Stellar mass is estimated by measuring the amount of light coming from old stars whose emission peaks at $\sim 1.6\,\mu$m in the rest-frame. Often, full model SEDs are fit to available photometry to obtain an estimate for stellar mass. Age and reddening affect the SED and so even though full fitting techniques might appear sophisticated, the stellar mass estimate is still uncertain and the results of studies with variable data quality can be difficult to directly compare. So instead, we use two simple methods of estimating stellar mass directly from the NIR rest-frame flux. First, following the approach of Daddi et al. (2004) the stellar mass is estimated from the K-band brightness together with a $(B-z)$ colour correction. This method can be applied to any BzK sample as it uses only the B-, z- and K-band data. Second, and perhaps more robustly, for galaxies with IRAC detections, we can estimate the $1.6\,\mu$m flux directly and calibrate that with stellar mass.

4.1.1 K-band technique

In Daddi et al. (2004), multi-wavelength photometry is fit with SED templates to estimate stellar mass and find a correlation between the SED-estimated stellar mass and observed K-band magnitude:

$$\log(M_\star/10^{11}M_\odot) = -0.4(K^{\rm tot} - K^{11}), \tag{4.1}$$

where $K^{11}_{\rm AB} = 21.34$. Though the K-band does not sample the rest-frame $1.6\,\mu$m stellar bump directly, Daddi et al. (2004) found that applying a colour correction term is sufficient to account for the bulk of the effects of reddening due to redshift and dust:

$$\Delta \log M_\star = 0.218((z-K)_{\rm AB} - 2.29). \tag{4.2}$$

4.1.2 1.6 μm stellar bump technique

The second, perhaps more intuitive method is to simply estimate the flux at 1.6 μm, the peak of the stellar bump, and then relate that to stellar mass through a single proportionality coefficient. This is a particularly effective and straightforward method when IRAC data and redshifts are available. Comparing νL_ν at 1.6 μm rest-frame to the K-band only stellar mass estimate described above, we obtain figure 4.1 and the conversion from νL_ν at 1.6 μm (rest-frame) to stellar mass is

$$\log M_\star[M_\odot] = 0.808 \log((\nu L_\nu)|_{1.6\,\mu\mathrm{m}}[\mathrm{W}]) + 2.080. \tag{4.3}$$

4.2 Star formation rates

Star formation rate (SFR) is a measure of the mass of stars forming per unit time, typically in units of solar masses per year. The general prescription for measuring SFR is to measure the amount of light coming from young stars and then use an initial mass function (IMF) to convert to mass of stars. Here, we use the rest-frame ultra-violet, mid-infrared and radio to estimate SFR for our sample of BzKs. The following SFR estimators only work for galaxies with $z \sim 2$, so we restrict our sample to the SBzKs with no hard X-ray detections and with redshifts in the desired range of $1.4 \leq z \leq 2.5$.

4.2.1 Ultra-violet

The rest-frame ultra-violet (UV, $\lambda \sim 900 - 3000$ Å) directly samples the peak emission of young, massive stars. The complication with estimating SFR from UV emission is that dust absorbs UV photons. Galaxies with high SFRs have high gas densities (Kennicutt, 1998) and so in general (for average metallicities), these galaxies have more dust attenuation. The timescale for which young, massive stars emit strongly in the UV is ~ 100 Myr (Calzetti, 2008b). Hence, the comparison between various wavelength SFR estimators can depend on the respective timescales and mass ranges sampled. Additionally, a more severe problem lies in calculating dust attenuation. However, a simple relationship between reddening and dust attenuation holds for starburst galaxies (Calzetti et al., 2000), which should be reliable for our actively star forming 'SBzK' sample.

Following Daddi et al. (2004) we use the B-band to sample the rest-frame UV. The B-band is centred at 4350Å, sampling rest-frame wavelengths ranging from $\sim 1800-1200$ Å for the BzK redshifts ($1.4 \leq z \leq 2.5$), with the

well-calibrated dust attenuation at 1500 Å (Madau et al., 1998) falling at our average redshift of 1.9. Daddi et al. (2007), found the following correlation between reddening estimated through full SED model fitting with the $(B-z)$ colour:

$$E(B-V) = 0.25(B-z+0.1)_{\rm AB}. \tag{4.4}$$

The attenuation factor for the appropriate rest-frame wavelength is found using the Calzetti extinction law (Calzetti et al., 2000), i.e. $A(1500\,\text{Å}) \simeq 10 \times E(B-V)$, where the B-band is centred at $\simeq 1500$ Å for $z = 1.9$. Finally, we assume that dereddening flattens the galaxies' spectra such that no K-correction is needed to obtain $L_\nu(1500\,\text{Å})$, which can therefore be converted to a star formation rate:

$$\text{SFR}(M_\odot\,\text{yr}^{-1}) = L_\nu(1500\,\text{Å})/(8.85 \times 10^{34}\text{W Hz}^{-1}). \tag{4.5}$$

The result is shown in figure 4.2. The sources with spectroscopic redshifts follow the relationship $\log(\text{SFR}[M_\odot\,\text{yr}^{-1}]) = 0.99 \times \log(M_\star/M_\odot) - 8.8$, while the sources with only photometric redshifts follow $\log(\text{SFR}[M_\odot\,\text{yr}^{-1}]) = 1.2 \times \log(M_\star/M_\odot) - 11$. The photometric redshift sample is offset from and shows much more scatter than the spectroscopic redshift sample which tightly follows the trend. This is likely due to the fact that the photometric redshifts artificially cluster at $z \sim 1.5$ and do not accurately represent the true redshift distribution (see figure 3.3 and section 3.3 for discussion). In this UV SFR method, since the B-band samples *around* 1500Å rest-frame, the skewed redshift distribution shows up as an offset in the SFR vs. stellar mass plot. For comparison with other SFR estimators in section 4.3, we use the spectroscopic redshift best-fit relationship.

4.2.2 Mid-infrared

As mentioned above, galaxies with higher SFRs are also dustier. The dust absorbs UV photons produced by young, massive stars and re-emits that radiation in the mid- and far-IR. The observed 24 μm flux density samples the rest-frame $\sim$ 8 μm emission. In the local universe, the relationship between 8 μm flux and SFR is known to depend on metallicity (Calzetti et al., 2007), but nevertheless we can estimate SFRs assuming an average metallicity.

In order to go from observed 24 μm flux density to SFR, we first estimate the total IR luminosity by fitting Chary and Elbaz templates (Chary & Elbaz, 2001). We then use the standard relationship from Kennicutt (1998):

$$\mathrm{SFR}(M_\odot\,\mathrm{yr}^{-1}) = (1.8 \times 10^{-10}) \times L_{\mathrm{IR}}(L_\odot). \quad (4.6)$$

The results are shown in figure 4.3. The sources with spectroscopic redshifts follow the relationship $\log(\mathrm{SFR}[M_\odot\,\mathrm{yr}^{-1}]) = 1.5 \times \log(M_\star/M_\odot) - 13$, while the sources with only photometric redshifts follow $\log(\mathrm{SFR}[M_\odot\,\mathrm{yr}^{-1}]) = 1.5 \times \log(M_\star/M_\odot) - 14$. These lines are in excellent agreement, showing this method is less sensitive to redshift distribution than the UV method. We use the spectroscopic redshift best-fit relation in section 3.3.

4.2.3 Radio

Although the radio emission does not directly trace star formation, there is a well-known correlation with the far-infrared. In order to use this we first find the rest-frame 1.4 GHz luminosity density. The rest-frame $\sim$ 1.4 GHz emission is synchrotron-dominated and so follows a power-law $S \propto \nu^{-\alpha}$ with a spectral index $\alpha \simeq -0.8$ (Condon, 1992). We use the conversion from rest-frame 1.4 GHz luminosity to total IR luminosity density described by Condon (1992) and refined by Yun et al. (2001):

$$L_{\mathrm{IR}}(\mathrm{L}_\odot) = (3.5 \times 10^{-12}) \times L_{1.4\,\mathrm{GHz}}(\mathrm{W\,Hz}^{-1}). \quad (4.7)$$

From the 1.4 GHz VLA radio map, we find 213 individual BzKs with significant radio detections, but only 44 have spectroscopic redshifts and many of the others have poorly constrained photometric redshifts. From these few detections, we obtain figure 4.4. The sources with spectroscopic redshifts follow the relationship $\log(\mathrm{SFR}[M_\odot\,\mathrm{yr}^{-1}]) = 0.85 \times \log(M_\star/M_\odot) - 6.5$, while the sources with only photometric redshifts follow $\log(\mathrm{SFR})M_\odot\,\mathrm{yr}^{-1}]) = 1.7 \times \log(M_\star/M_\odot) - 16$. In this case, the best-fit relations do not match well for the objects with spectroscopic redshifts and photometric redshifts, but since there are so few objects, this difference is insignificant.

For the many BzKs without radio detections, we can stack at their locations in the radio map to find their average flux. We can then use the average redshift, $z = 1.9$, to estimate the SFR from the stacking analysis, including the extended GOODS-N region to maximize the number of objects. We use the K-band method for estimating stellar mass since IRAC data do not exist for this extended region. This BzK sample is sufficiently large that we can split it up into five bins of stellar mass. In order to obtain detections in as many bins as possible, we create bins with approximately equal total mass, with the lower mass bins having many more objects than the higher mass bins. Stacking analysis was carried out by Glenn Morrison.

Figure 4.5 shows the stacking results for those objects with no radio detections compared to the binned average for objects with detections and then the combined average. The binned averages for the radio detections follow the relationship $\log(\mathrm{SFR}[M_\odot\,\mathrm{yr}^{-1}]) = 0.59 \times \log(M_\star/M_\odot) - 3.2$. The stacked non-detections follow $\log(\mathrm{SFR}[M_\odot\,\mathrm{yr}^{-1}]) = 0.84 \times \log(M_\star/M_\odot) - 7.2$. And the combined average follows $\log(\mathrm{SFR}[M_\odot\,\mathrm{yr}^{-1}]) = 1.4 \times \log(M_\star/M_\odot) - 12$. We use the best-fit relation for the combined average in section 4.3.

4.3 Comparing various SFR estimators

The three methods to estimate star formation rate described above are compared in figure 4.6. We show the UV and mid-IR SFR relations for galaxies with spectroscopic redshifts and the combined average (binned detections + stacked non-detections) for the radio. We then compare our multi-wavelength results with the relation found in Daddi et al. (2007) for a comparable BzK sample in GOODS-S. They find the SFR stellar mass relation following $\log(\mathrm{SFR}[M_\odot\,\mathrm{yr}^{-1}]) = 0.9 \times \log(M_\star/M_\odot) - 7.6$. Our three relations follow the same general trend as the Daddi et al. (2007) line, but none match precisely. Since the selection techniques and SFR estimation methods were consistent with the previous work, we conclude that high redshift SFR estimators have intrinsic uncertainties and cannot be constrained further without detailed spectroscopic follow-up to determine AGN contamination and possible SED evolution.

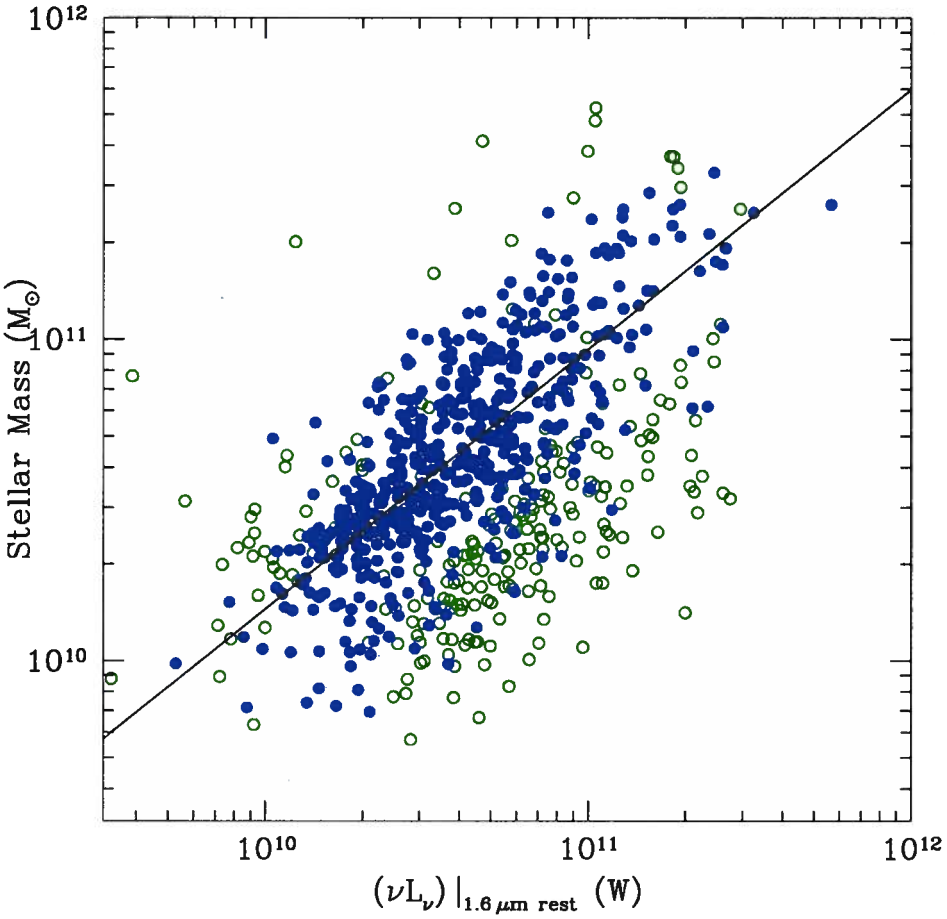

Figure 4.1: Comparison of νL_ν at 1.6 μm rest-frame to the K-band only stellar mass estimate for the BzKs with IRAC detections and redshifts. Green points are outside the $1.4 \leq z \leq 2.5$ redshift range for which the K-band only method was calibrated. We set our conversion to stellar mass (equation 4.3) using only the blue points; this is shown by the solid line.

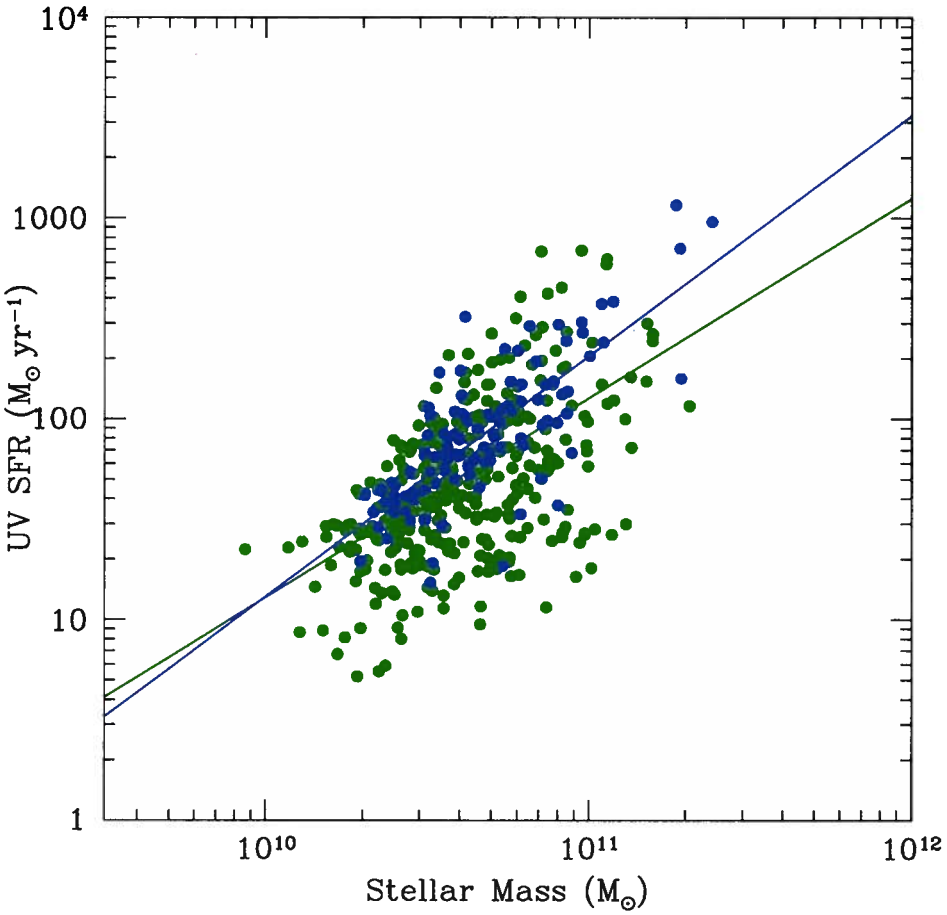

Figure 4.2: Ultra-violet star formation rate versus stellar mass. Blue points are objects with spectroscopic redshifts, green points are objects with only photometric redshifts and the lines are best fit relationships for each group of objects. The offset between objects with photometric redshifts and those with spectroscopic redshifts is likely due to the artifically large spike in photometric redshift distribution at $z = 1.5$.

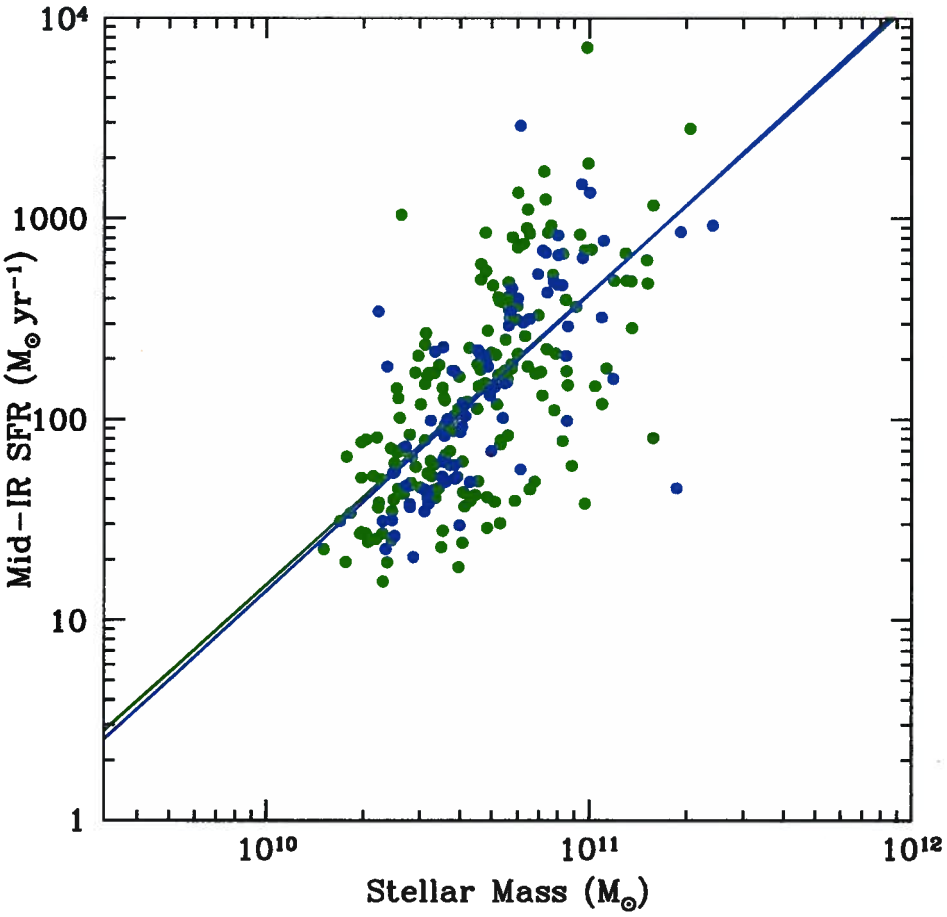

Figure 4.3: Mid-infrared star formation rate versus stellar mass. Blue points are objects with spectroscopic redshifts, green points are objects with only photometric redshifts and the lines are best-fit relationships for each group of objects. The two sets of objects agree very well.

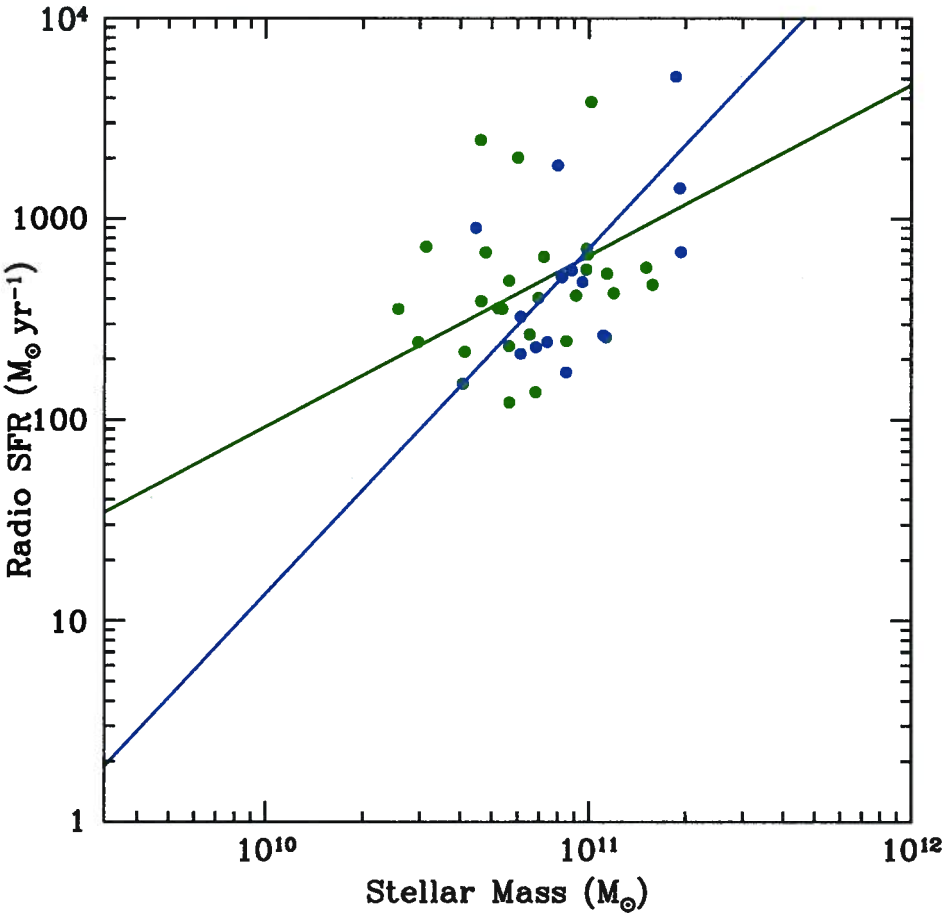

Figure 4.4: Radio star formation rate versus stellar mass for objects with individual radio detections. Blue points are objects with spectroscopic redshifts, green points are objects with only photometric redshifts and the lines are best fit relationships for each group of objects. There are too few sources to rely on the best fit relationships here; stacking analysis allows us to make more progress, as described in Section 4.2.3.

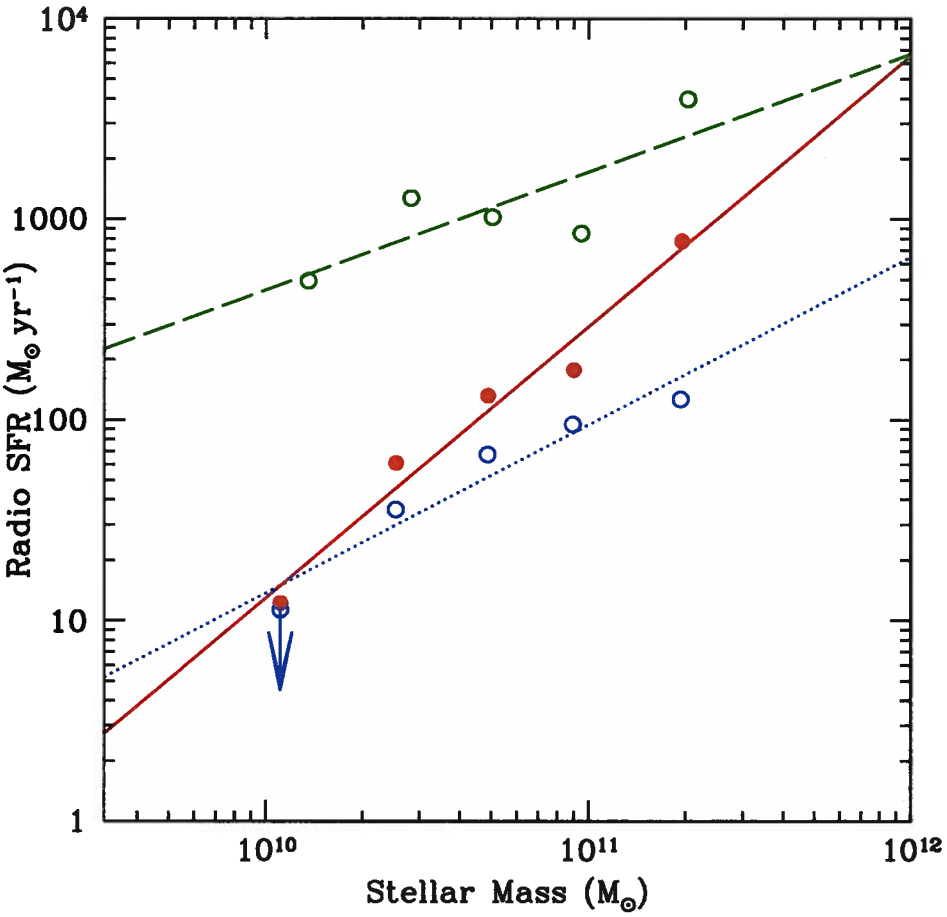

Figure 4.5: Binned radio star formation rate versus stellar mass. The binned detections are shown in green, stacked non-detections are in blue and the combined average is in red.

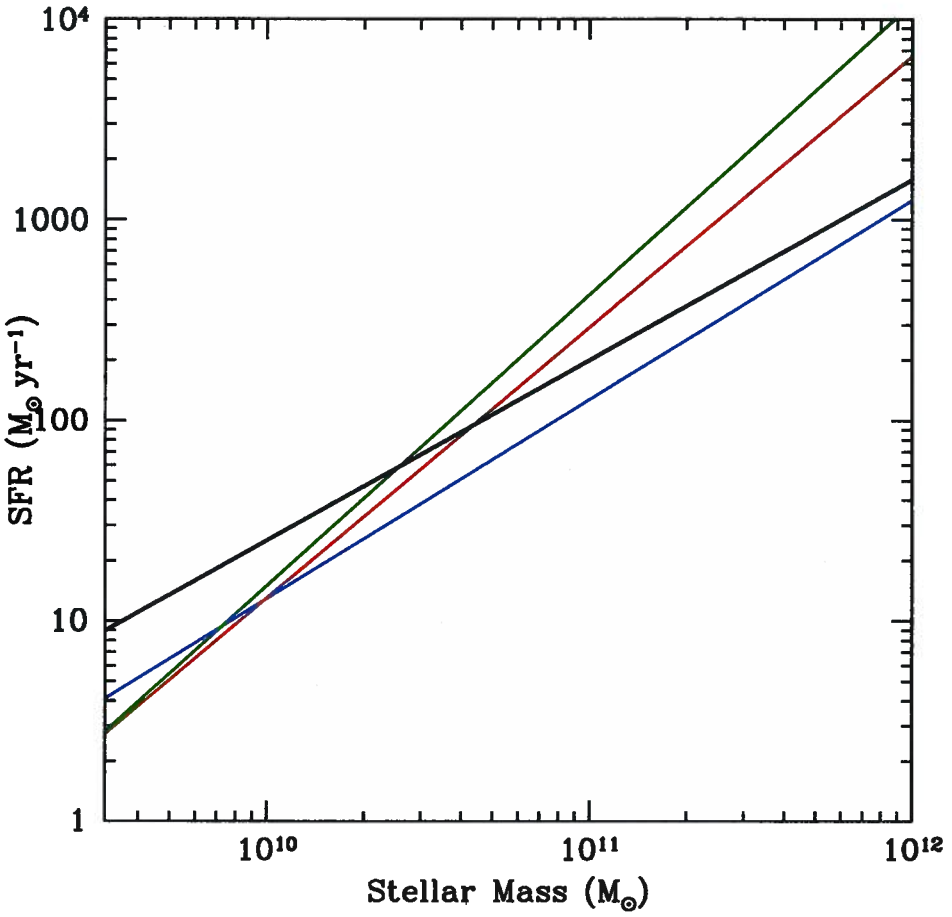

Figure 4.6: Comparison of SFR estimators described above: UV in blue, Mid-IR in green and Radio in red. The black line is the relationship found in Daddi et al. (2007) for BzKs in GOODS-S. All lines follow a common trend and scatter is likely due to the uncertain nature of high redshift SFR estimators.

Chapter 5

Comparing various $z \sim 2$ galaxy populations

We can compare our sample selection to other $z \sim 2$ populations to test how robust the BzK criterion works. Two relevant galaxy populations are the high star forming submillimetre galaxies and the very red dust obscured galaxies. Considering these extreme galaxies within the BzK framework helps us evaluate the robustness of the selection criterion.

5.1 Submillimetre galaxies

Submillimetre galaxies (SMGs) are a population of galaxies which are ultra luminous in the infrared (e.g. Chapman et al., 2005). Pope et al. (2006) used GOODS-N SCUBA imaging at 850 μm to obtain a sample of 36 objects with a redshift distribution peaking at $z = 2$ (Pope et al., 2006). They found SMGs to have $L_{\rm IR} \simeq 6.0 \times 10^{12}\,{\rm L}_{\odot}$, translating to SFR $\sim 1100\,M_{\odot}\,{\rm yr}^{-1}$ by equation 4.6.

Using the SMG sample, we search our K-band catalogue for sources within $1''$ of an SMG. Of the 36 SMGs in GOODS-N, 32 are detected in K with $\geq 3\sigma$ (GN03, GN09, GN10 and GN21 are not detected). These galaxies are plotted on the BzK diagram in figure 5.1. The specific classification and redshift information are given in table 5.1. Of the 32 SMGs with K detections, 17 would be classified as BzKs (though 4 would be removed, as they are detected in the hard X-ray). Of the 15 not classified as BzKs, 14 are outside the $1.4 \leq z \leq 2.5$ BzK redshift range (only GN12 is inside the redshift range but not classified as a BzK). The BzK selection has no problem including these objects with extremely high SFR if they are in the appropriate redshift range.

5.2 Dust Obscured Galaxies

Another galaxy population which is luminous in the infrared is the dust obscured galaxies (DOGs, Dye et al., 2008). These galaxies are detected with MIPS 24 μm imaging and are selected for their extreme rest-frame mid-IR to UV flux ratios. The DOG selection criterion requires $S_{24\,\mu\mathrm{m}}/S_R > 1000$, selected to be more extreme than any type of galaxy in the local Universe. As discussed in chapter 4, dust absorbs UV photons from star formation or AGN and emits in the infrared. Thus, a high mid-IR to UV flux is indicative of an extrememly dusty galaxy. DOGs have a redshift distribution centred at $z = 2$ (Dye et al., 2008; Fiore et al., 2008; Pope et al., 2008). The BzK criterion is designed to select galaxies independant of dust content. Therefore, examining the extremely dusty DOG population in the BzK plane is an important test of this aspect of the selection technique.

Using the available MIPS 24 μm data and the Subaru R-band imaging, we select DOGs in figure 5.2. We find 108 galaxies satisfying the DOG criterion and 102 of these have significant K-band detections. These DOGs are plotted on the BzK diagram in figure 5.3 and nearly all the DOGs lie in the BzK region. They are not all *formally* identified as BzKs, since 16 have hard X-ray detections and many are not detected in B, making definitive classification challenging. However, in general, the BzK criterion is very successful at identifying these extremely dusty high redshift galaxies.

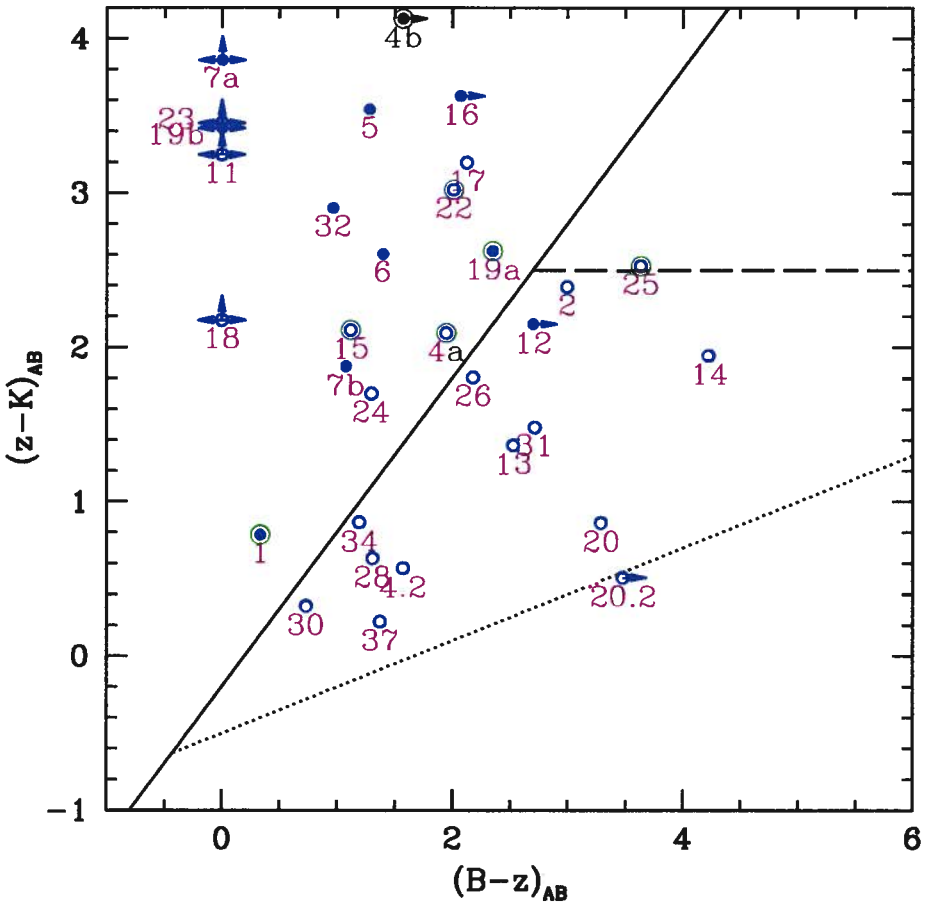

Figure 5.1: The Pope et al. (2006) SMGs on the BzK diagram. Open points are outside the $1.4 \leq z \leq 2.5$ BzK redshift range and hard X-ray detections are circled in green. SMG IDs match those in table 5.1.

SMG ID	BzK type	redshift	Hard X-ray detection
GN01	SBzK	2.415	Y
GN02		(1.29)	N
GN04a	SBzK	2.578	Y
GN04b	UBzK	(2.27)	Y
GN05	SBzK	(2.41)	N
GN06	SBzK	1.865	N
GN07a	UBzK	1.992	N
GN07b	SBzK	1.988	N
GN11	UBzK	(4.14)	N
GN12		2.003	N
GN13		0.475	N
GN14		(1.10)	Y
GN15	SBzK	2.743	N
GN16	UBzK	(1.89)	N
GN17	SBzK	0.884	N
GN18		(2.89)	N
GN19a	SBzK	2.490	N
GN19b	UBzK	(1.85)	N
GN20		(0.44)	N
GN22	SBzK	2.505	Y
GN23	UBzK	(3.90)	N
GN24	SBzK	(3.07)	N
GN25		1.013	Y
GN26		1.219	N
GN28		1.019	N
GN30		1.355	N
GN31		0.935	N
GN32	SBzK	(2.05)	N
GN34		1.363	N
GN37		3.189	N
GN04.2		0.851	N
GN20.2		(4.03)	N

Table 5.1: BzK description of GOODS-N SMGs (Pope et al., 2006). Redshifts in parentheses are photometric estimates.

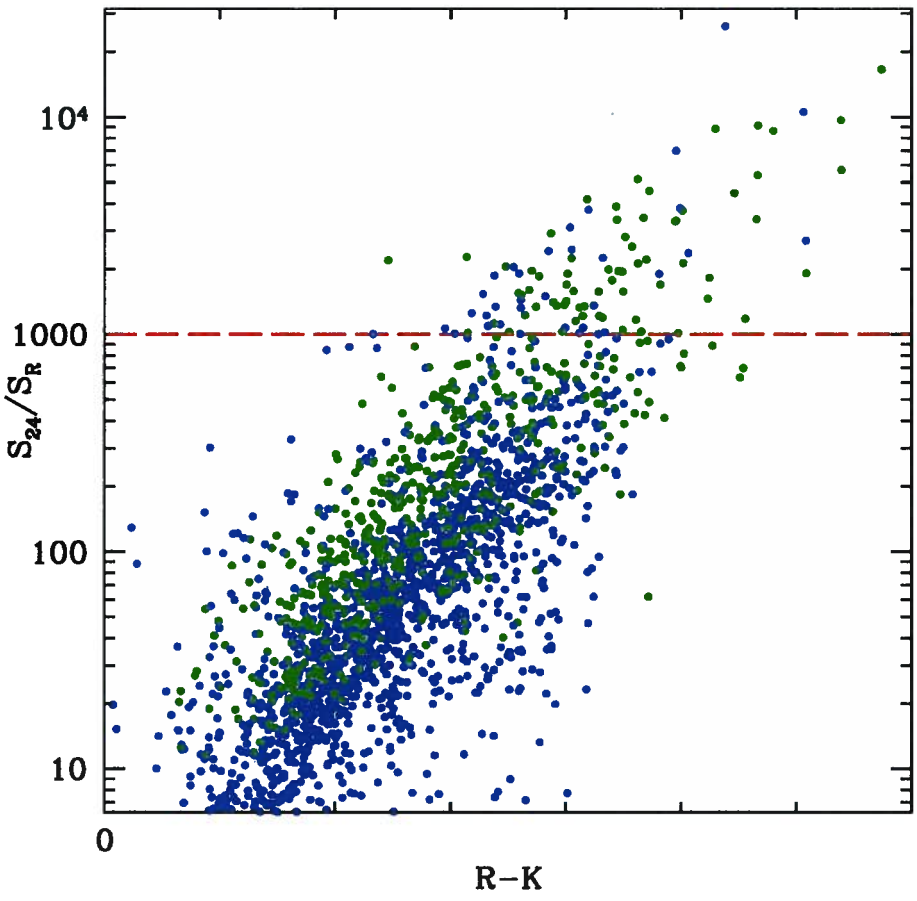

Figure 5.2: The DOG selection requires $S_{24\,\mu m}/S_R > 1000$ (above the dashed red line). The whole GOODS-N sample is shown in blue, with BzKs in green.

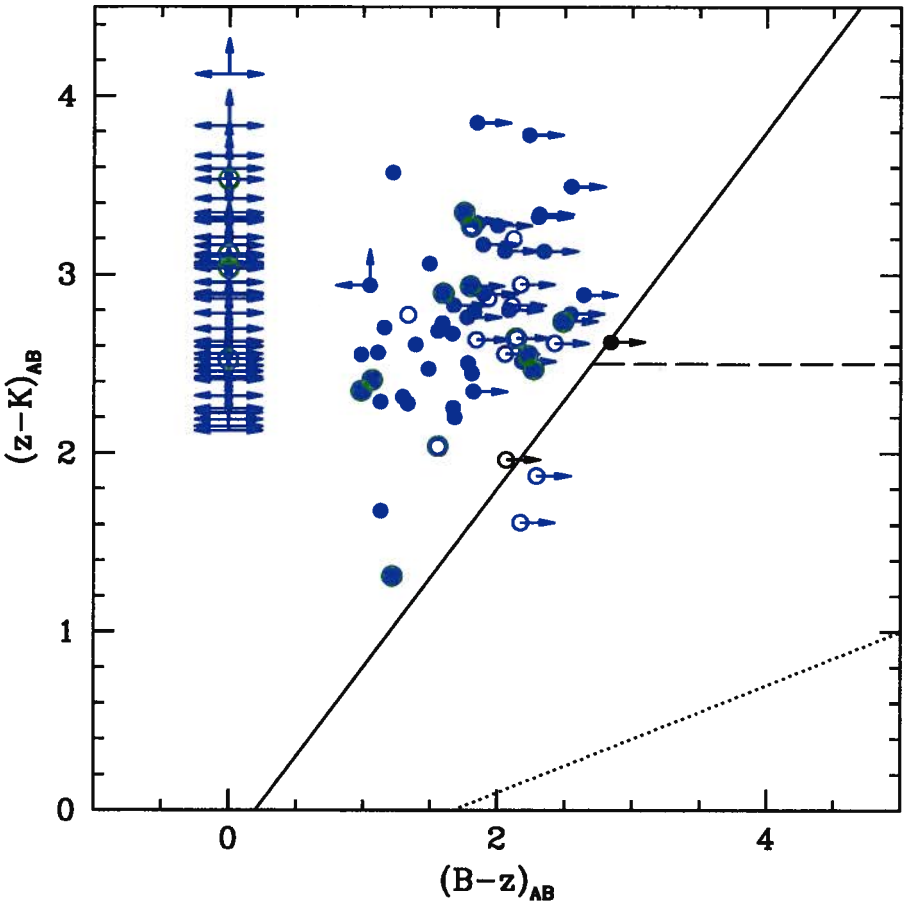

Figure 5.3: Dust obscured galaxies on the BzK diagram. Open circles are DOGs outside the $1.4 \leq z \leq 2.5$ BzK redshift range. Hard X-ray sources are circled in green.

Chapter 6

Conclusion

Prior to this thesis project, GOODS-N lacked deep NIR data. That gap in the multi-wavelength coverage of GOODS-N has now been filled with J- and K-band imaging from WIRCam on CFHT. We have improved the data reduction process to remove severe crosstalk artifacts, ensure accurate astrometry and produce science-grade photometry. We have produced a source catalogue which has already been used for published results (Pope et al., 2008).

With our source catalogue, we are able to select a deep sample of $z \sim 2$ galaxies with the BzK selection technique. Our sample rivals those of the deepest BzK studies ($K(\mathrm{AB}) \leq 23.8$). We use the extensive catalogue of publicly available spectroscopic redshifts to investigate the redshift distribution for this deep BzK sample. We find that the deep sample follows the desired BzK redshift range of $1.4 \leq z \leq 2.5$ very well, with only 13% contamination from low redshift interlopers. We also present a new photometric redshift catalogue using our NIR data. Using these photometric redshifts to further investigate the redshift distribution of BzKs we find only 14% low redshift contamination. Note that although many high redshift galaxies are included in our BzK photometric redshift sample, it is unclear whether these galaxies are truly at such high redshifts or if our photometric redshift catalogue breaks down at these redshifts.

We adopt a straightforward approach to estimating stellar mass by simply measuring the luminosity at $1.6\,\mu$m (rest-frame), at the peak of old stellar emission. We then estimate star formation rates in three different ways, with the rest-frame UV to sample young stellar emission, the mid-IR to sample the emission from dust heated by star formation and the radio coming from cosmic ray electrons, which correlates to the far-IR dust emission. Comparing these multi-wavelength star formation rate tracers, we find that though these techniques follow similar trends, their detailed normalizations are difficult to constrain. In particular, the UV method is sensitive to the redshift distribution. The mid-IR method is known from local studies to have severe metallicity dependance, but works relatively well for our sample. With the radio, even using a very deep radio map, stacking analysis is re-

quired. In general, our results agree with previous work, though the scatter among the three methods shows the imprecise nature of high redshift star formation measurements. In particular, it is difficult to remove AGN contamination and there is the possibility that SED templates developed from observations of local galaxies are not applicable at high redshifts.

Finally, we compare the BzK selection technique with other $z \sim 2$ galaxy populations. We find that the BzK criterion is able to select the ultra luminous infrared submillimetre detected galaxies with $1.4 \leq z \leq 2.5$ even though these galaxies have extremely high star formation rates. Also, extremely dust obscured galaxies are all consistent with BzKs though by definition they are difficult to detect in the optical wavebands.

Bibliography

Alexander, D. M., Bauer, F. E., Brandt, W. N., Garmire, G. P., Hornschemeier, A. E., Schneider, D. P., & Vignali, C., 2003, *Astronomische Nachrichten* 324, 8

Baldry, I. K., Glazebrook, K., Budavári, T., Eisenstein, D. J., Annis, J., Bahcall, N. A., Blanton, M. R., Brinkmann, J., Csabai, I., Heckman, T. M., Lin, H., Loveday, J., Nichol, R. C., & Schneider, D. P., 2005, *M.N.R.A.S.* 358, 441

Bertin, E. & Arnouts, S., 1996, *Astron. Astrophys. Suppl. Ser.* 117, 393

Bond, J. R., Kofman, L., & Pogosyan, D., 1996, *Nature* 380, 603

Bruzual, G. & Charlot, S., 2003, *M.N.R.A.S.* 344, 1000

Calzetti, D., 2008a, *ArXiv e-prints*

Calzetti, D., 2008b, in J. H. Knapen, T. J. Mahoney, & A. Vazdekis (eds.), *Pathways Through an Eclectic Universe*, Vol. 390 of *Astronomical Society of the Pacific Conference Series*, pp 121–+

Calzetti, D., Armus, L., Bohlin, R. C., Kinney, A. L., Koornneef, J., & Storchi-Bergmann, T., 2000, *Ap.J.* 533, 682

Calzetti, D., Kennicutt, R. C., Engelbracht, C. W., Leitherer, C., Draine, B. T., Kewley, L., Moustakas, J., Sosey, M., Dale, D. A., Gordon, K. D., Helou, G. X., Hollenbach, D. J., Armus, L., Bendo, G., Bot, C., Buckalew, B., Jarrett, T., Li, A., Meyer, M., Murphy, E. J., Prescott, M., Regan, M. W., Rieke, G. H., Roussel, H., Sheth, K., Smith, J. D. T., Thornley, M. D., & Walter, F., 2007, *Ap.J.* 666, 870

Capak, P., Cowie, L. L., Hu, E. M., Barger, A. J., Dickinson, M., Fernandez, E., Giavalisco, M., Komiyama, Y., Kretchmer, C., McNally, C., Miyazaki, S., Okamura, S., & Stern, D., 2004, *A.J.* 127, 180

Chapman, S. C., Blain, A. W., Smail, I., & Ivison, R. J., 2005, *Ap.J.* 622, 772

Chary, R. & Elbaz, D., 2001, *Ap.J.* 556, 562

Cohen, J. G., Hogg, D. W., Blandford, R., Cowie, L. L., Hu, E., Songaila, A., Shopbell, P., & Richberg, K., 2000, *Ap.J.* 538, 29

Condon, J. J., 1992, 30, 575

Cowie, L. L., Barger, A. J., Hu, E. M., Capak, P., & Songaila, A., 2004, *A.J.* 127, 3137

Cowie, L. L., Songaila, A., Hu, E. M., & Cohen, J. G., 1996, *A.J.* 112, 839

Daddi, E., Cimatti, A., Renzini, A., Fontana, A., Mignoli, M., Pozzetti, L., Tozzi, P., & Zamorani, G., 2004, *Ap.J.* 617, 746

Daddi, E., Dickinson, M., Morrison, G., Chary, R., Cimatti, A., Elbaz, D., Frayer, D., Renzini, A., Pope, A., Alexander, D. M., Bauer, F. E., Giavalisco, M., Huynh, M., Kurk, J., & Mignoli, M., 2007, *Ap.J.* 670, 156

Dunne, L., Ivison, R. J., Maddox, S., Cirasuolo, M., Mortier, A. M., Foucaud, S., Ibar, E., Almaini, O., Simpson, C., & McLure, R., 2008, *ArXiv e-prints* 808

Dye, S., Eales, S. A., Aretxaga, I., Serjeant, S., Dunlop, J. S., Babbedge, T. S. R., Chapman, S. C., Cirasuolo, M., Clements, D. L., Coppin, K. E. K., Dunne, L., Egami, E., Farrah, D., Ivison, R. J., van Kampen, E., Pope, A., Priddey, R., Rieke, G. H., Schael, A. M., Scott, D., Simpson, C., Takagi, T., Takata, T., & Vaccari, M., 2008, *M.N.R.A.S.* 386, 1107

Elston, R., Raines, S. N., Hanna, K. T., Hon, D. B., Julian, J., Horrobin, M., Harmer, C. F. W., & Epps, H. W., 2003, in M. Iye & A. F. M. Moorwood (eds.), *Society of Photo-Optical Instrumentation Engineers (SPIE) Conference Series*, Vol. 4841 of *Society of Photo-Optical Instrumentation Engineers (SPIE) Conference Series*, pp 1611–1624

Elston, R., Rieke, G. H., & Rieke, M. J., 1988, *Ap.J. (Letters)* 331, L77

Erb, D. K., Shapley, A. E., Steidel, C. C., Pettini, M., Adelberger, K. L., Hunt, M. P., Moorwood, A. F. M., & Cuby, J.-G., 2003, *Ap.J.* 591, 101

Fiore, F., Grazian, A., Santini, P., Puccetti, S., Brusa, M., Feruglio, C., Fontana, A., Giallongo, E., Comastri, A., Gruppioni, C., Pozzi, F., Zamorani, G., & Vignali, C., 2008, *Ap.J.* 672, 94

Giavalisco, M., Ferguson, H. C., Koekemoer, A. M., Dickinson, M., Alexander, D. M., Bauer, F. E., Bergeron, J., Biagetti, C., Brandt, W. N., Casertano, S., Cesarsky, C., Chatzichristou, E., Conselice, C., Cristiani, S., Da Costa, L., Dahlen, T., de Mello, D., Eisenhardt, P., Erben, T., Fall, S. M., Fassnacht, C., Fosbury, R., Fruchter, A., Gardner, J. P., Grogin, N., Hook, R. N., Hornschemeier, A. E., Idzi, R., Jogee, S., Kretchmer, C., Laidler, V., Lee, K. S., Livio, M., Lucas, R., Madau, P., Mobasher, B., Moustakas, L. A., Nonino, M., Padovani, P., Papovich, C., Park, Y., Ravindranath, S., Renzini, A., Richardson, M., Riess, A., Rosati, P., Schirmer, M., Schreier, E., Somerville, R. S., Spinrad, H., Stern, D., Stiavelli, M., Strolger, L., Urry, C. M., Vandame, B., Williams, R., & Wolf, C., 2004, *Ap.J. (Letters)* 600, L93

Greve, T. R., Pope, A., Scott, D., Ivison, R. J., Borys, C., Conselice, C. J., & Bertoldi, F., 2008, *M.N.R.A.S.* 389, 1489

Kennicutt, Jr., R. C., 1998, 36, 189

Lilly, S. J., Le Fevre, O., Hammer, F., & Crampton, D., 1996, *Ap.J. (Letters)* 460, L1+

Madau, P., Ferguson, H. C., Dickinson, M. E., Giavalisco, M., Steidel, C. C., & Fruchter, A., 1996, *M.N.R.A.S.* 283, 1388

Madau, P., Pozzetti, L., & Dickinson, M., 1998, *Ap.J.* 498, 106

Moorwood, A., Cuby, J.-G., Biereichel, P., Brynnel, J., Delabre, B., Devillard, N., van Dijsseldonk, A., Finger, G., Gemperlein, H., Gilmozzi, R., Herlin, T., Huster, G., Knudstrup, J., Lidman, C., Lizon, J.-L., Mehrgan, H., Meyer, M., Nicolini, G., Petr, M., Spyromilio, J., & Stegmeier, J., 1998, *The Messenger* 94, 7

Oke, J. B., 1974, *Ap.J. (Suppl)* 27, 21

Peacock, J. A., 1999, *Cosmological Physics*, Cosmological Physics, by John A. Peacock, pp. 704. ISBN 052141072X. Cambridge, UK: Cambridge University Press, January 1999.

Perera, T. A., Chapin, E. L., Austermann, J. E., Scott, K. S., Wilson, G. W., Halpern, M., Pope, A., Scott, D., Yun, M. S., Lowenthal, J. D., Morrison, G., Aretxaga, I., Bock, J. J., Coppin, K., Crowe, M., Frey, L., Hughes, D. H., Kang, Y., Kim, S., & Mauskopf, P. D., 2008, *ArXiv e-prints*

Pérez-González, P. G., Rieke, G. H., Villar, V., Barro, G., Blaylock, M., Egami, E., Gallego, J., Gil de Paz, A., Pascual, S., Zamorano, J., & Donley, J. L., 2008, *Ap.J.* 675, 234

Pope, A., Bussmann, R. S., Dey, A., Meger, N., Alexander, D. M., Brodwin, M., Chary, R.-R., Dickinson, M. E., Frayer, D. T., Greve, T. R., Huynh, M., Lin, L., Morrison, G., Scott, D., & Yan, C.-H., 2008, *ArXiv e-prints* 808

Pope, A., Scott, D., Dickinson, M., Chary, R.-R., Morrison, G., Borys, C., Sajina, A., Alexander, D. M., Daddi, E., Frayer, D., MacDonald, E., & Stern, D., 2006, *M.N.R.A.S.* 370, 1185

Puget, P., Stadler, E., Doyon, R., Gigan, P., Thibault, S., Luppino, G., Barrick, G., Benedict, T., Forveille, T., Rambold, W., Thomas, J., Vermeulen, T., Ward, J., Beuzit, J.-L., Feautrier, P., Magnard, Y., Mella, G., Preis, O., Vallee, P., Wang, S.-y., Lin, C.-J., Hall, D. N., & Hodapp, K. W., 2004, in A. F. M. Moorwood & M. Iye (eds.), *Society of Photo-Optical Instrumentation Engineers (SPIE) Conference Series*, Vol. 5492 of *Society of Photo-Optical Instrumentation Engineers (SPIE) Conference Series*, pp 978–987

Reddy, N. A., Erb, D. K., Steidel, C. C., Shapley, A. E., Adelberger, K. L., & Pettini, M., 2005, *Ap.J.* 633, 748

Reddy, N. A., Steidel, C. C., Erb, D. K., Shapley, A. E., & Pettini, M., 2006, *Ap.J.* 653, 1004

Reddy, N. A., Steidel, C. C., Pettini, M., Adelberger, K. L., Shapley, A. E., Erb, D. K., & Dickinson, M., 2008, *Ap.J. (Suppl)* 175, 48

Sajina, A., Lacy, M., & Scott, D., 2005, *Ap.J.* 621, 256

Salpeter, E. E., 1955, *Ap.J.* 121, 161

Sawicki, M., 2002, *A.J.* 124, 3050

Skrutskie, M. F., Cutri, R. M., Stiening, R., Weinberg, M. D., Schneider, S., Carpenter, J. M., Beichman, C., Capps, R., Chester, T., Elias, J.,

Huchra, J., Liebert, J., Lonsdale, C., Monet, D. G., Price, S., Seitzer, P., Jarrett, T., Kirkpatrick, J. D., Gizis, J. E., Howard, E., Evans, T., Fowler, J., Fullmer, L., Hurt, R., Light, R., Kopan, E. L., Marsh, K. A., McCallon, H. L., Tam, R., Van Dyk, S., & Wheelock, S., 2006, *A.J.* 131, 1163

Spergel, D. N., Bean, R., Doré, O., Nolta, M. R., Bennett, C. L., Dunkley, J., Hinshaw, G., Jarosik, N., Komatsu, E., Page, L., Peiris, H. V., Verde, L., Halpern, M., Hill, R. S., Kogut, A., Limon, M., Meyer, S. S., Odegard, N., Tucker, G. S., Weiland, J. L., Wollack, E., & Wright, E. L., 2007, *Ap.J. (Suppl)* 170, 377

Steidel, C. C., Giavalisco, M., Dickinson, M., & Adelberger, K. L., 1996, *A.J.* 112, 352

Thompson, R. I., Eisenstein, D., Fan, X., Dickinson, M., Illingworth, G., & Kennicutt, Jr., R. C., 2006, *Ap.J.* 647, 787

Wirth, G. D., Willmer, C. N. A., Amico, P., Chaffee, F. H., Goodrich, R. W., Kwok, S., Lyke, J. E., Mader, J. A., Tran, H. D., Barger, A. J., Cowie, L. L., Capak, P., Coil, A. L., Cooper, M. C., Conrad, A., Davis, M., Faber, S. M., Hu, E. M., Koo, D. C., Le Mignant, D., Newman, J. A., & Songaila, A., 2004, *A.J.* 127, 3121

York, D. G., Adelman, J., Anderson, Jr., J. E., Anderson, S. F., Annis, J., Bahcall, N. A., Bakken, J. A., Barkhouser, R., Bastian, S., Berman, E., Boroski, W. N., Bracker, S., Briegel, C., Briggs, J. W., Brinkmann, J., Brunner, R., Burles, S., Carey, L., Carr, M. A., Castander, F. J., Chen, B., Colestock, P. L., Connolly, A. J., Crocker, J. H., Csabai, I., Czarapata, P. C., Davis, J. E., Doi, M., Dombeck, T., Eisenstein, D., Ellman, N., Elms, B. R., Evans, M. L., Fan, X., Federwitz, G. R., Fiscelli, L., Friedman, S., Frieman, J. A., Fukugita, M., Gillespie, B., Gunn, J. E., Gurbani, V. K., de Haas, E., Haldeman, M., Harris, F. H., Hayes, J., Heckman, T. M., Hennessy, G. S., Hindsley, R. B., Holm, S., Holmgren, D. J., Huang, C.-h., Hull, C., Husby, D., Ichikawa, S.-I., Ichikawa, T., Ivezić, Ž., Kent, S., Kim, R. S. J., Kinney, E., Klaene, M., Kleinman, A. N., Kleinman, S., Knapp, G. R., Korienek, J., Kron, R. G., Kunszt, P. Z., Lamb, D. Q., Lee, B., Leger, R. F., Limmongkol, S., Lindenmeyer, C., Long, D. C., Loomis, C., Loveday, J., Lucinio, R., Lupton, R. H., MacKinnon, B., Mannery, E. J., Mantsch, P. M., Margon, B., McGehee, P., McKay, T. A., Meiksin, A., Merelli, A., Monet, D. G., Munn, J. A., Narayanan, V. K., Nash, T., Neilsen, E., Neswold, R., Newberg, H. J., Nichol, R. C., Nicinski, T., Nonino, M., Okada, N., Okamura, S., Ostriker, J. P., Owen, R., Pauls,

A. G., Peoples, J., Peterson, R. L., Petravick, D., Pier, J. R., Pope, A., Pordes, R., Prosapio, A., Rechenmacher, R., Quinn, T. R., Richards, G. T., Richmond, M. W., Rivetta, C. H., Rockosi, C. M., Ruthmansdorfer, K., Sandford, D., Schlegel, D. J., Schneider, D. P., Sekiguchi, M., Sergey, G., Shimasaku, K., Siegmund, W. A., Smee, S., Smith, J. A., Snedden, S., Stone, R., Stoughton, C., Strauss, M. A., Stubbs, C., SubbaRao, M., Szalay, A. S., Szapudi, I., Szokoly, G. P., Thakar, A. R., Tremonti, C., Tucker, D. L., Uomoto, A., Vanden Berk, D., Vogeley, M. S., Waddell, P., Wang, S.-i., Watanabe, M., Weinberg, D. H., Yanny, B., & Yasuda, N., 2000, *A.J.* 120, 1579

Yun, M. S., Reddy, N. A., & Condon, J. J., 2001, *Ap.J.* 554, 803